AWARD NUMBER: **W81XWH-20-1-0113**

TITLE: A New In Situ Cryo-Electron Microscopy Approach to Directly Visualize Mutations in Mitochondrial Disease

PRINCIPAL INVESTIGATOR: Zachary Freyberg, M.D., Ph.D.

CONTRACTING ORGANIZATION: University of Pittsburgh, Pittsburgh, PA

REPORT DATE: March 2021

TYPE OF REPORT: Annual Technical Report

PREPARED FOR: U.S. Army Medical Research and Materiel Command
Fort Detrick, Maryland 21702-5012

REPORT DOCUMENTATION PAGE

Form Approved
OMB No. 0704-0188

1. REPORT DATE	2. REPORT TYPE	3. DATES COVERED
March 2021	Annual Report	01Mar2020 – 28Feb2021

4. TITLE AND SUBTITLE

A New In Situ Cryo-Electron Microscopy Approach to Directly Visualize Mutations in Mitochondrial Disease

5a. CONTRACT NUMBER
W81XWH-20-1-0113

5b. GRANT NUMBER
PR192466

5c. PROGRAM ELEMENT NUMBER

6. AUTHOR(S)
Zachary Freyberg M.D., Ph.D.

E-Mail: freyberg@pitt.edu

5d. PROJECT NUMBER

5e. TASK NUMBER

5f. WORK UNIT NUMBER

7. PERFORMING ORGANIZATION NAME(S) AND ADDRESS(ES)

University of Pittsburgh
3520 Fifth Avenue
Pittsburgh, PA 15213-3320

8. PERFORMING ORGANIZATION REPORT NUMBER

9. SPONSORING / MONITORING AGENCY NAME(S) AND ADDRESS(ES)

U.S. Army Medical Research and Materiel Command
Fort Detrick, Maryland 21702-5012

10. SPONSOR/MONITOR'S ACRONYM(S)

11. SPONSOR/MONITOR'S REPORT NUMBER(S)

12. DISTRIBUTION / AVAILABILITY STATEMENT

Approved for Public Release; Distribution Unlimited

13. SUPPLEMENTARY NOTES

14. ABSTRACT

Mitochondrial dysfunction is associated with several chronic, deployment-associated conditions in Veterans. *In situ* cryo-electron tomography (cryo-ET) imaging is a new 3D imaging approach that we have used to study patient cells with unprecedented detail. Our goal is to test the feasibility of cryo-ET to visualize mitochondrial structural changes in patient cells. We hypothesize *in situ* cryo-ET will resolve structural changes in the individual mitochondrial respiratory complexes and organization of these complexes into higher-order supercomplexes. We have now obtained primary fibroblast cells from patients with distinct mitochondrial complex I mutations including ND6, ACAD9, and NDUFV1 subunits and optimized growing these mutant cells on EM grids. We characterized effects of these mutations on mitochondrial morphology and dynamics in living patient cells. *In situ* cryo-ET revealed disruptions of mitochondrial inner membranes and crista morphology distinct to each mutant. Our results suggest these respiratory complex subunits are key regulators of overall mitochondrial structure and function and their disruption directly alters their function to produce profound human disease.

15. SUBJECT TERMS

16. SECURITY CLASSIFICATION OF:			17. LIMITATION OF ABSTRACT	18. NUMBER OF PAGES	19a. NAME OF RESPONSIBLE PERSON
a. REPORT	b. ABSTRACT	c. THIS PAGE			USAMRMC
Unclassified	Unclassified	Unclassified	Unclassified	33	19b. TELEPHONE NUMBER *(include area code)*

Table of Contents

1. INTRODUCTION

Mitochondrial diseases are often caused by mutations that disrupt structures of the mitochondrial respiratory complexes, significantly impairing mitochondrial function. Substantial numbers of people are also affected by mitochondrial dysfunction associated with prevalent diseases including diabetes, Alzheimer's disease, and Parkinson's disease. The combined impact of these mitochondrial impairments is enormous. Mitochondrial dysfunction is suspected in a variety of chronic, deployment-associated conditions in Veterans or in association with Gulf War Illness (GWI). For example, exposure to neurotoxicants including pesticides (*e.g.*, Agent Orange, permethrin, paraquat) and airborne hazards in military theater have been negatively associated with Veterans' health post-deployment. Yet, the precise mechanisms remain poorly understood. Our ability to accurately diagnose disturbances in mitochondrial function remains profoundly limited. Current diagnostic approaches test mitochondrial function (*i.e.*, respiration) and cannot resolve specific disease-causing mitochondrial structural defects despite evidence of broader mitochondrial dysfunction. Such approaches are often invasive and may alter the appearance of mitochondria, hindering accurate diagnosis. Thus, there is great clinical need for more accurate diagnostic approaches since better diagnosis will translate to improved patient outcomes. *In situ* cryo-electron tomography (cryo-ET) imaging is a new three-dimensional (3D) imaging approach to visualize disease-induced changes in mitochondrial structure directly in primary human patient cells for the first time. The unprecedented resolution provided by cryo-ET can visualize alterations in respiratory complex structures unique to the disease-causing mutations and/or acquired mitochondrial defects. We previously used *in situ* cryo-ET to identify profound structural changes in mitochondria within primary fibroblasts from a patient with Leigh Syndrome (LS), a debilitating mitochondrial disease. The structural alterations, produced by a novel mutation, have not been previously identified via conventional imaging, illustrating the power of this approach. We therefore hypothesize that: (**A**) *In situ* cryo-ET will visualize distinct structural changes both in the individual mitochondrial respiratory complexes and organization of the complexes into larger, higher-order assemblies termed supercomplexes. These visualized altered structures will explain the loss of functional efficiency and metabolic flux in complexes as evidenced in mitochondrial disease mutations, GWI, or exposures to pesticides and PB. (**B**) Drugs that improve respiratory chain function can correct structural abnormalities of supercomplex organization, providing the basis for novel therapies. To test these hypotheses, we aim to do the following: (**1**) To determine the effects of disease-causing mutations on individual mitochondrial respiratory complexes and higher-order supercomplex organization *in situ*; and (**2**) To identify effects of GWI and associated neurotoxicants on respiratory chain complex structure and higher-order organization *in situ* in patient cells. We have established new experimental systems where we have grown primary cells taken from patients directly on EM grids followed by imaging of the mitochondria within these cells via *in situ* cryo-ET to resolve disease-induced changes to mitochondrial structure and morphology. We have also developed novel drugs like JP4-039 that improve mitochondrial function in affected patient cells potentially through their actions on mitochondrial respiratory complex structure. In the short term, we expect that our proposed *in situ* cryo-EM studies will reveal mitochondrial structural alterations that disrupt mitochondrial respiratory complex structures in response to GWI or neurotoxicant exposures affecting Veterans. This may form the basis for new, highly accurate and non-invasive diagnostic approaches for mitochondrial disease. In the longer term, our studies will serve as a foundation for future work that leads to new, highly targeted personalized therapies for active military, Veterans and the general population that are directed at correcting structural changes responsible for mitochondrial dysfunction.

2. KEYWORDS

Keywords relevant to the work proposed here include:

1. Mitochondrial disease
2. Cryo-electron tomography
3. Respiratory complex
4. Supercomplex
5. Pesticide
6. Gulf War Illness

3. ACCOMPLISHMENTS

- **What were the major goals of the project?**
  The major goals of the project are as follows:

1) Sample preparation and imaging acquisition of three-dimensional tomograms from mitochondrial disease patient and control cells.
2) Analysis of imaged mitochondria and respiratory complexes from well-defined mitochondrial disease mutation-containing patient and control fibroblasts.
3) Determine whether the respective mitochondrial disease-causing mutations alter the 3D structures of the mitochondrial respiratory complexes *in situ.*
4) Determine whether improved respiratory chain function in patient cells following treatment with JP4-039 is via the drug's ability to correct respiratory complex structural abnormalities.
5) Visualize mitochondrial respiratory complex structure and supercomplex organization in healthy primary human fibroblasts after pesticide or pyridostigmine bromide (PB) treatment.
6) Determine whether JP4-039 corrects mitochondrial structural abnormalities in GWI or pesticide/PB-treated control cells.

- **What was accomplished under these goals?**
  In the course of the reporting period for Year 1 of this award, we conducted studies to address major goals of the project as follows:

I. Sample preparation and imaging acquisition of three-dimensional tomograms from mitochondrial disease patient and control cells.

- We have successfully received IACUC and IRB approval for all of our proposed work during this reporting period.
- We have optimized the culture conditions to grow primary fibroblasts acquired directly from patients with primary mitochondrial diseases containing well-defined disease-causing mutations in the following respiratory complex I subunits: ND6, ACAD9, NDUFV1; we also optimized the culturing of a respiratory complex V mutant responsible for causing Leigh Syndrome (LS). In parallel, we have also established the culturing conditions for primary fibroblasts acquired from the healthy control subjects. Moreover, we can now culture these cells directly on EM grids which we have subsequently plunge-frozen to vitrify the respective cells, preserving them in a near-native state.
- We have successfully imaged the above mitochondrial respiratory complex I mutants and the control cells via *in situ* cryo-ET and acquired 3D tomograms for each of the mutations. Moreover, in our mitochondrial complex V (ATP synthase) mutant-containing patient fibroblasts, we imaged through the depth of entire cell via serial cryo-focused ion beam milling and scanning electron microscopy (cryo-FIB/SEM) for the first time. This enabled us to generate a complete 3D reconstruction of the cell.

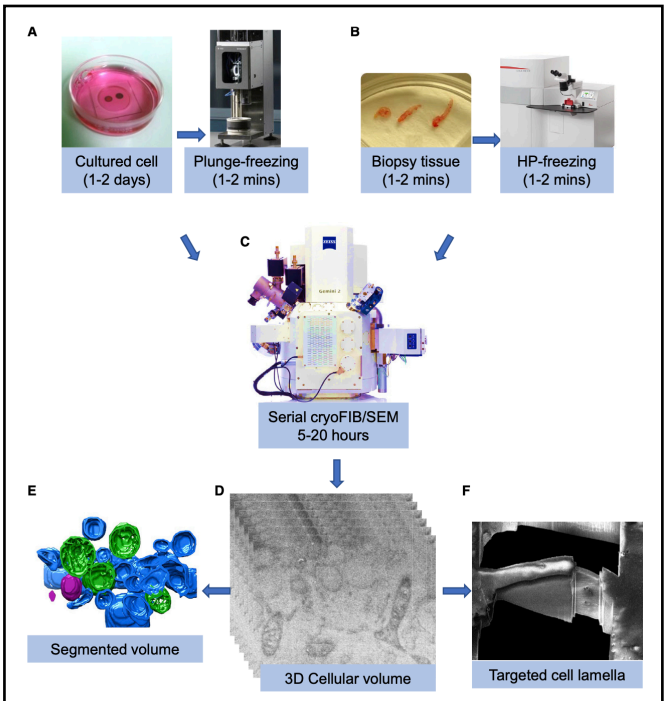

Fig. 1. Workflow for serial cryo-FIB/SEM volume imaging of cells and tissues in near-native states. Cells cultured directly on EM grids and then plunge-frozen **(A)** or tissues acquired by needle biopsy and immediately high-pressure frozen **(B)** undergo serial cryo-FIB/SEM **(C)**, followed by cryo-imaging to produce a 3D cellular volume of the whole cell or tissue region **(D)**. 3D volumes are segmented **(E)** and, in parallel, targeted cell lamellae can be prepared on intracellular regions of interest **(F)**.

II. Analysis of imaged mitochondria and respiratory complexes from well-defined mitochondrial disease mutation-containing patient and control fibroblasts.

- We recently adopted serial FIB/scanning electron microscopy (SEM) technology to generate large 3D volumes of cells and tissues (Zhu *et al.*, Structure 2021). Unlike conventional cryo-FIB-milling which generates thinned lamellae of an individual cell subregion, serial cryo-FIB/SEM can image much larger volumes of frozen-hydrated cells and tissues. As proof-of-principle, we devised a sample preparation and imaging workflow that enabled us to visualize an entire frozen-hydrated primary human fibroblast from a patient with a disease-causing mutation in the USMG5 protein within the respiratory complex V. The USMG5 protein is critical for dimerizing the ATP synthase complex and the inability to dimerize results in Leigh Syndrome, an often-fatal mitochondrial disease (**Figure 1**). Combining large-scale cryo-volume imaging with cryo-ET has now enabled us to map whole cells and tissues in both healthy states as well as in pathological states of mitochondrial disease. Notably, in the USMG5 mutant cells, we discovered substantial cytoarchitectural derangements, with the interior of the cell largely occupied by vacuolated structures of indeterminate origin. Of the residual identifiable structures, including mitochondria and Golgi apparatus, organelles are significantly decreased in volume and display gross morphological abnormalities. For example, the Golgi apparatus lacks extended membrane stacks (**Figure 2**). More remarkably, compared with the complex shape and network of mitochondria in the control cell (**Figures 2A, 2G, and 2H**), nearly all patient mitochondria are roughly round with minimal cristae (**Figures 2J, 2L, and 2N**), consistent with our previous cryoET analyses (Siegmund *et al.*, iScience 2018). Ultimately, these data strongly suggest that the architecture responsible for energy metabolism in the patient cells is

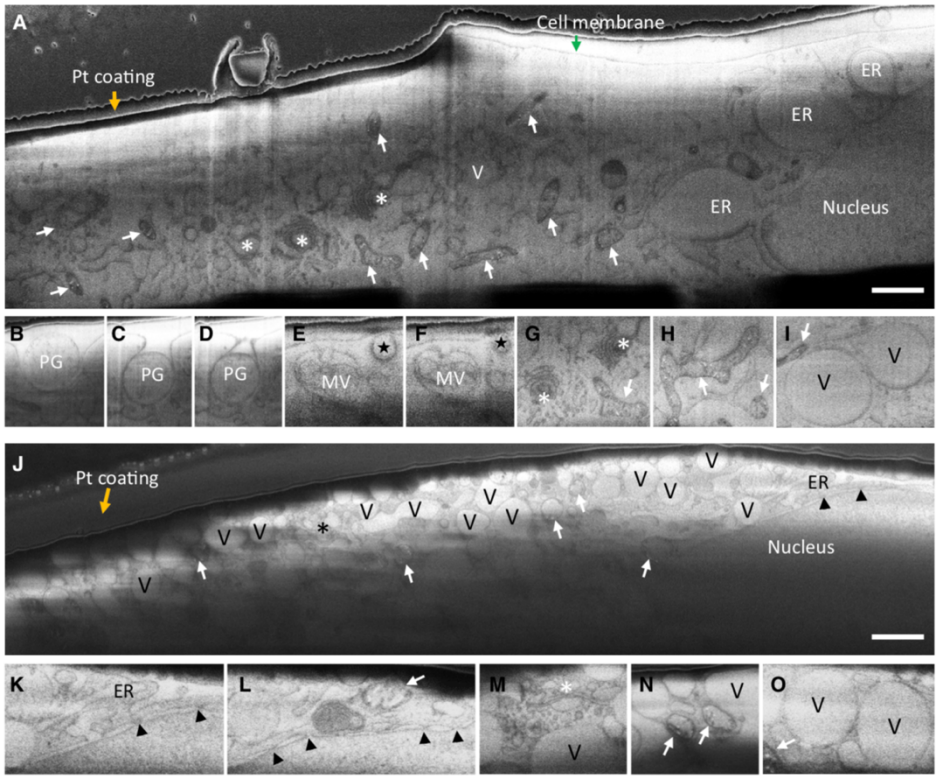

Fig. 2. Serial cryoFIB/SEM of frozen-hydrated primary fibroblast cells from a Leigh Syndrome patients and unaffected control. (A) Representative cryoSEM image from a stack of 575 serial micrographs recorded from a control fibroblast cell cultured on an EM grid. **(B–I)** Image gallery of subcellular structures and organelles observed in the control cell, including three consecutive slices of a phagosome entering the cell (B–D), two consecutive slices of an endosome (E and F, star), a multivesicular body (E and F, MV), Golgi complexes (G, asterisks), tubular-shaped mitochondria (G and H, arrow), and vacuoles (I and V). **(J)** A representative cryoSEM image from a stack of 2018 serial micrographs recorded from a patient fibroblast cell cultured on an EM grid. **(K–O)** An image gallery of subcellular structures and organelles observed in the patient cell, showing endoplasmic reticulum (K, ER), nuclear pores (K and L, arrowheads), Golgi complex (M, asterisk), mitochondria (L and N, arrows), and vacuoles (M, O, and V). Arrows, mitochondria; asterisks, Golgi; stars, endosome; PG, phagosome; MV, multivesicular body; V, vacuoles; arrowheads, nuclear pore; orange arrows, platinum GIS coating; green arrow, cell membrane; ER, endoplasmic reticulum. Scale bars, 1 mm.

compromised in response to a single disease-causing mutation within just one mitochondrial respiratory complex.

- Building on our work investigating complex V mutant cells, we have made significant progress in visualizing mitochondria affected by mitochondrial disease-causing mutations in additional respiratory complexes including complex I directly in the cells of patients as well as in unaffected controls. As noted above, we focused on the following mitochondrial disease-causing complex I mutants:
    - **ND6 mutant:** ND6 is a mitochondrial chromosome-encoded structural subunit of complex I embedded in the inner mitochondrial membrane.
    - **NDUFV1 mutant:** NDUFV1 is a nuclear-encoded subunit of complex I that forms part of the NADH binding domain that extends into the mitochondrial matrix.
    - **ACAD9 mutant:** ACAD9 is a complex I assembly factor, and mutations within this protein lead to a complete deficiency of fully-assembled complex I.

As an initial step in imaging the distinct complex I mutants, we first characterized the respective mutant patient cells at the light level via live-cell confocal microscopy, labeling the mitochondria with MitoTracker Deep Red dye (**Figure 3**).

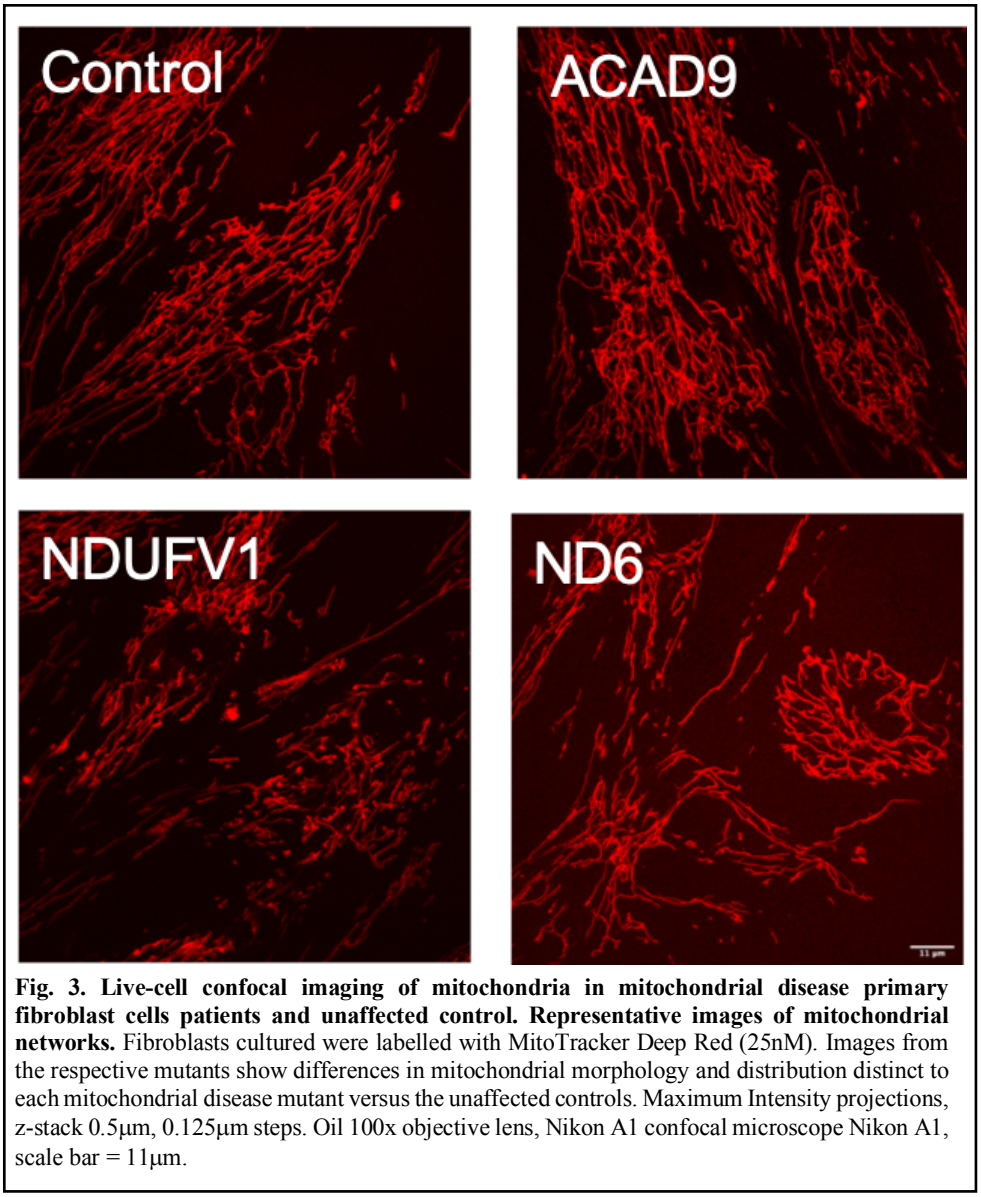

Fig. 3. Live-cell confocal imaging of mitochondria in mitochondrial disease primary fibroblast cells patients and unaffected control. Representative images of mitochondrial networks. Fibroblasts cultured were labelled with MitoTracker Deep Red (25nM). Images from the respective mutants show differences in mitochondrial morphology and distribution distinct to each mitochondrial disease mutant versus the unaffected controls. Maximum Intensity projections, z-stack 0.5µm, 0.125µm steps. Oil 100x objective lens, Nikon A1 confocal microscope Nikon A1, scale bar = 11µm.

- Analysis of our live-imaging data revealed that, compared to the unaffected control fibroblasts, each of the disease-causing respiratory complex I mutants exhibits significant morphological differences that are distinct at the light-level. To determine precisely how the respective respiratory complex mutations alter mitochondrial biology, we established a pipeline for analysis of mitochondrial morphology from our live-imaging data. Using Nikon NIS Elements software, we were able to measure parameters including total network length, longest component, number of components, and average length of components by performing a 3D skeletonization of mitochondrial networks (n=5-6 images per genotype) (**Figures 4**). Upon quantification of our imaging results, we discovered that both NDUFV1 and ND6 mutants exhibit significant decreases in the length of the mitochondrial networks compared to unaffected controls (**Figure 4A**). Likewise, the NDUFV1 and ND6 mutants have diminished length of the longest individual components within their networks (**Figure 4B**). In contrast, NDUFV1 mutants demonstrate a significantly increased number of total network components (**Figure 4C**). Lastly, we found that the overall length of the components of the mitochondrial networks were diminished in the NDUFV1 and ND6 mutants (**Figure 4D**).

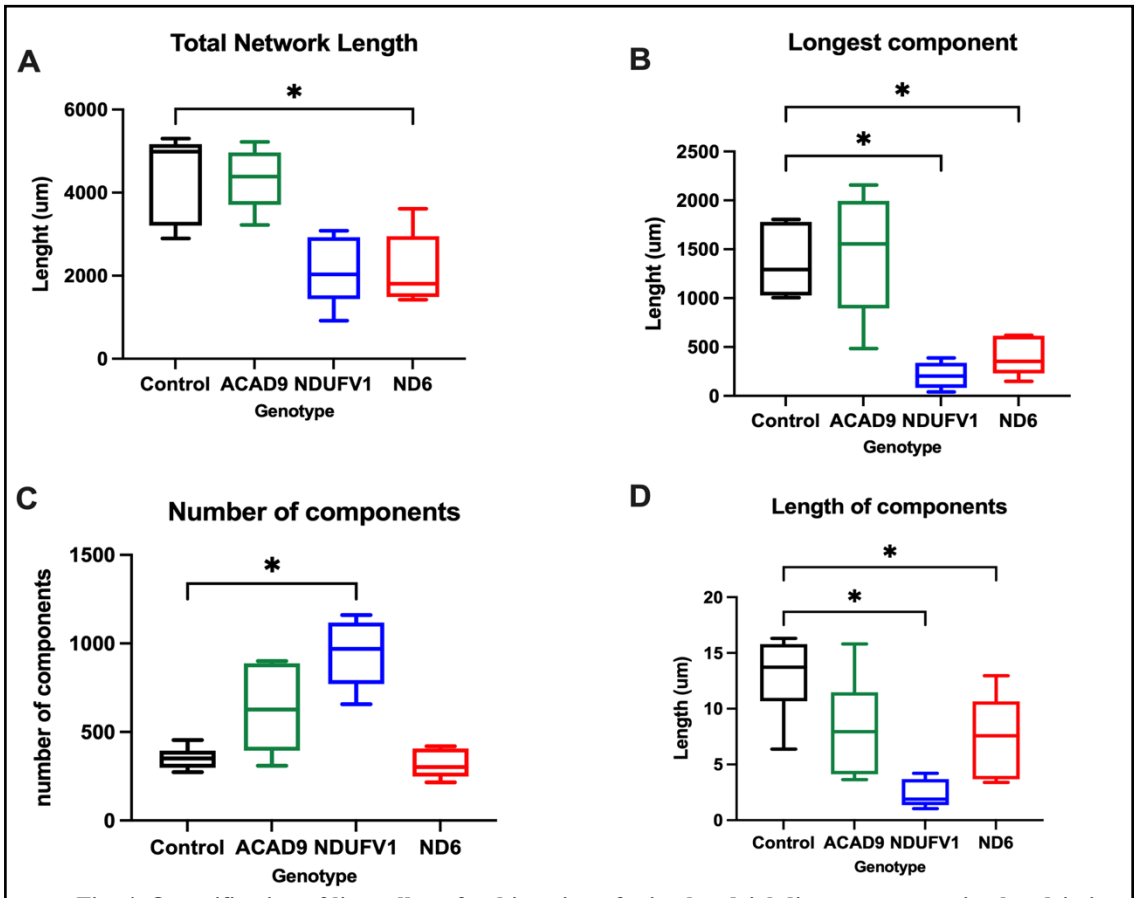

Fig. 4. Quantification of live-cell confocal imaging of mitochondrial disease mutant mitochondria in primary fibroblast cells patients and unaffected control. Quantification of mitochondria within the respective patient fibroblasts revealed that the NDUFV1 and ND6 respiratory complex I mutants exhibited significant differences in mitochondrial organization and network arrangements including decreases in (**A**) total network length, (**B**) component length, (**C**) number of components for the NDUFV1 mutant, and (**D**) the total length of the components. Quantification used n=5-6 images per genotype. Data is represented a mean ± SEM of percentage change as compared to average of measurements in the control line normalized to 100%.

In parallel to our live-imaging studies, we have begun imaging using *in situ* cryo-ET, taking advantage of this approach's much higher resolution to visualize effects of the disease-causing mutations on mitochondrial structure. We first focused on the ACAD9 and ND6 mutant cells (**Figure 5**). Consistent with our live-imaging studies, cryo-ET imaging revealed prominent morphological and structural disturbances in mitochondria imaged within both ACAD9 and ND6 mutant fibroblasts. We found a substantial reduction in visible cristae in ACAD9 mutant mitochondria (**Figure 5A**), and a near-complete absence of cristae in ND6 mutant mitochondria (**Figure 5B**). Additionally, in both ACAD9 and ND6 mutants, we discovered more numerous and/or much larger calcium phosphate granules distributed throughout the mitochondrial matrix compared to our previous descriptions of healthy human mitochondria (see Siegmund *et al.*, iScience 2018). Since elevated mitochondrial calcium levels are known to increase generation of reactive oxygen species, these increases in calcium phosphate granule numbers and size may indicate broader mitochondrial dysfunction (Adam-Vizi and Starkov, J Alz Dis 2011); our further work will determine whether this possibility is indeed the case. Moreover, these data suggest that dysfunctional respiratory complex I subunits may play a role in mitochondrial calcium homeostasis, providing a potentially new therapeutic target.

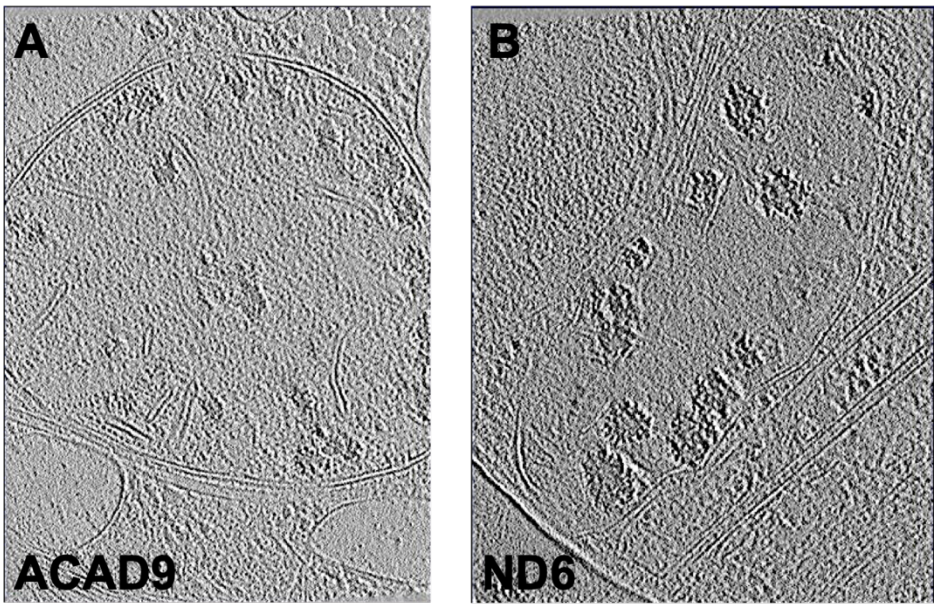

Fig. 5. Visualization of mitochondrial disease-causing respiratory complex mutations on mitochondrial structures in primary fibroblast cells of patients. Representative 2D images taken from reconstructed 3D tomograms of mitochondria from ACAD9 **(A)** and ND6 **(B)** respiratory complex I mutant patient fibroblasts. We find substantial reductions in cristae, as well as increases in the numbers of electron-dense calcium phosphate granules in both ACAD9 and ND6 mutant mitochondria. Notably, the size of the calcium phosphate granules in the ND6 mutant mitochondria also appear enlarged relative to the granules within ACAD9 mutant mitochondria.

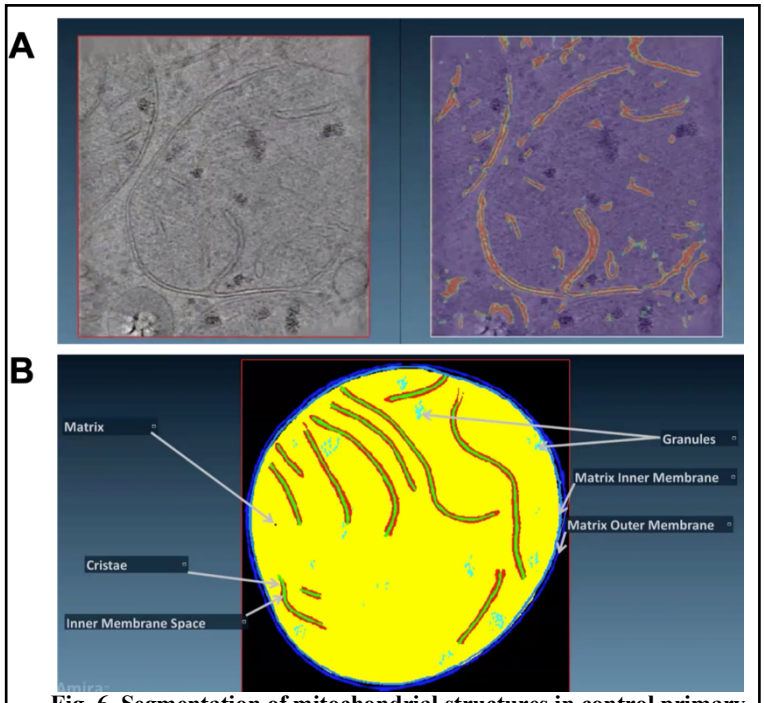

Fig. 6. Segmentation of mitochondrial structures in control primary fibroblast cells. (A) Segmentation of 2D cryo-ET images of mitochondria from unaffected control fibroblasts (left panel) using machine learning-based approaches demonstrated recognition of distinct membrane structures (right panel). **(B)** Using these segmented data, we were able to accurately segment mitochondria including cristae and calcium phosphate granules.

III. Determine whether the respective mitochondrial disease-causing mutations alter the 3D structures of the mitochondrial respiratory complexes *in situ*.

- We have begun segmenting mutant and control mitochondria reconstructed from the three-dimensional (3D) *in situ* cryo-tomography data acquired from respective patient and control primary fibroblast cells. We are testing machine learning approaches to rapidly and accurately identify mitochondrial membranes during the segmentation process (**Figure 6A**). Consequently, we have successfully applied these methods to rapidly and accurately identify the mitochondrial inner and outer membranes, including the cristae in our control unaffected mitochondria (**Figure 6B**). This paves the way for quantification of potential derangements to the mitochondrial structure using 2D and 3D measurements including inner membrane surface area and volume, cristae length and cristae tip angles. We successfully segmented mitochondria from cryo-tomograms acquired in the ND6 mutant patient fibroblasts (**Figure 7**). Our segmentation data confirm marked reduction in cristae number and size (**Figures 7A & B**) and dramatic increases in the number and size of calcium phosphate granules within the mutant mitochondria (**Figures 7B & C**). Work is currently ongoing to segment the complete mutant and control datasets and to use these data for quantification of membrane alterations as noted above.

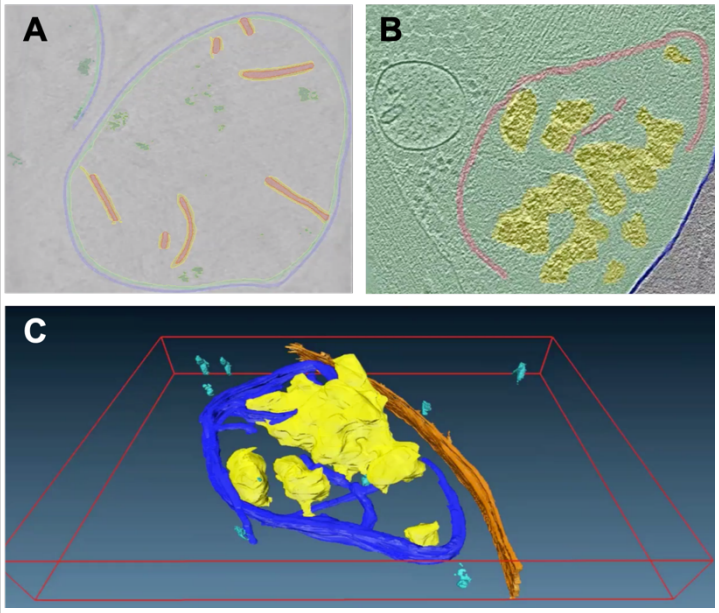

Fig. 7. Segmentation of mitochondrial structures in ND6 mutant primary patient fibroblast cells. (A) Segmentation of 2D cryo-ET images of mitochondria from ND6 fibroblasts reveal low numbers of cristae (in orange). **(B)** ND6 mutant mitochondria also have large clusters of calcium phosphate granules (in yellow). **(C)** 3D segmentation of a whole ND6 mutant mitochondrion showing altered membrane architecture (in blue), accumulations of calcium phosphate (in yellow); the segmented mitochondrion associates with microtubules (in orange).

- We have continued our collaboration with Dr. Min Xu (Carnegie Mellon University) to continue building more effective and rapid subtomogram averaging approaches to resolve the structures of the individual respiratory complexes as well as the higher-order supercomplexes *in situ* within the patient and control mitochondria. Together, we have been testing Dr. Xu's newly designed machine learning approaches for template-free structural pattern mining to facilitate unbiased detection of mitochondrial proteins and complexes extracted from our cryo-ET images. These techniques include: (a) fast, accurate subtomogram alignment; (b) reference-free macromolecule classification based on subtomogram alignment and averaging with cloud computing implementation, 3D rotational invariant features, pose normalization via supervised and unsupervised deep learning; (c) reference-free and reference-guided subtomogram segmentation; and (d) multiple and single structural pattern pursuit. For proof-of-concept, we successfully recovered patterns from numerous cellular structures within *in situ* cryo-tomograms including mitochondria (**Figure 8**).

IV. Determine whether improved respiratory chain function in patient cells following treatment with JP4-039 is via the drug's ability to correct respiratory complex structural abnormalities. We are currently validating the drug dose of JP4-039 to use for our live-cell and cryo-ET imaging studies. Once we determine the optimal dose, we will begin the imaging studies in the respective patient and control cells.

V. Visualize mitochondrial respiratory complex structure and supercomplex organization in healthy primary human fibroblasts after pesticide or pyridostigmine bromide treatment.

- We intend on co-administering pesticide and pyridostigmine in the next 6-8 months to our healthy

human fibroblasts followed by cryo-ET imaging to resolve effects of the drugs on respiratory complex structure and organization.

VI. Determine whether JP4-039 corrects mitochondrial structural abnormalities in GWI or pesticide/ pyridostigmine bromide-treated control cells.

- Our recent progress in resolving effects of the mitochondrial disease-causing mutations on mitochondrial structure and morphology in patient cells will lay the groundwork for visualizing effects of JP4-039 on the respiratory complex structures via cryo-ET. We expect to conduct these experiments in the next 12 months.

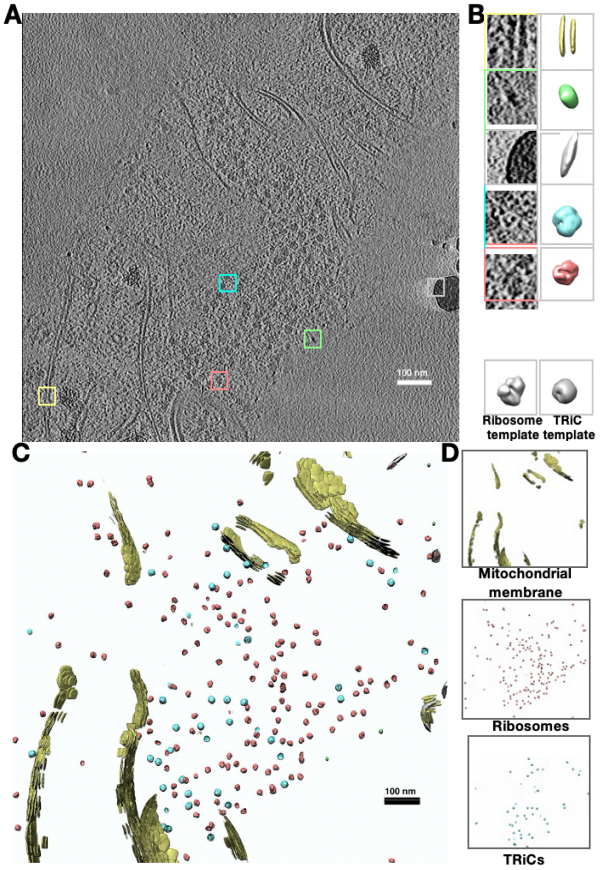

Fig. 8. Reference-free structural pattern mining. (A) original cryo-tomogram; **(B)** Recovered patterns (from top to bottom): mitochondrial membrane, ellipsoid of strong signals, borders of ice crystal, TRiC-like pattern, ribosome-like pattern. **(C)** Pattern mining results embedded. **(D)** Individual patterns embedded.

- **What opportunities for training and professional development has the project provided?**

Nothing to Report.

- **How were the results disseminated to communities of interest?**

Our results have been disseminated to communities of interest at national and international scientific meetings. These meetings include the Annual Meeting of the American Society of Cell Biology (2020) and the Annual American Physical Society Meeting (2021). Additionally, results were presented as an invited speaker at Weill Cornell Medical College's Department of Biochemistry (2020). Collectively, presenting recent findings stemming from this project were instrumental in advancing the idea that *in situ* cryo-ET offers a new approach towards better understanding and treating mitochondrial diseases by identifying how these illnesses alter mitochondrial structure and morphology. In presenting this work during talks, and abstracts, our findings were broadly disseminated to a broad scientific audience whose expertise spans multiple disciplines including neuroscience, cell biology, biophysics, and clinical medicine. Furthermore, publications detailing our results from this project were published in *Structure*, a high-impact journal of structural biology. In addition to the work already published, we presently have three manuscripts under preparation based on work resulting from this award. We expect to submit these manuscripts in the next 12 months.

- **What do you plan to do during the next reporting period to accomplish the goals?**

I. Sample preparation and imaging acquisition of three-dimensional tomograms from mitochondrial disease patient and control cells.

- We will continue culturing the primary human fibroblasts acquired from patients with well-defined mitochondrial diseases including those in complex I. In the next phase of studies, the respective fibroblast cells will be pre-treated with either JP4-039 or vehicle control followed by immediate plunge-freezing and vitrification of the samples.
- Once frozen, we will continue imaging the respective EM grids by *in situ* cryo-ET to obtain three-dimensional cryo-tomograms for further analysis of the patient and control cells.

II. Imaging Analysis of imaged mitochondria and respiratory complexes from well-defined mitochondrial disease mutation-containing patient and control fibroblasts.

- We will continue working with consultant Dr. Min Xu to develop new computational approaches using machine learning (ML) to recognize 3D respiratory complex structures *in situ* in mitochondria within patient and control cells. Structures from our data sets will be compared to high resolution structures of the respiratory complexes. These approaches will include auto-picking algorithms to accelerate the recognition and selection of the protein components of the mitochondrial respiratory complexes.
- We will continue segmenting structures within disease-altered complexes as well as the membrane organization (*i.e.*, cristae, inner and outer membranes) and then place the segmented structures back into tomograms to determine spatial relationships between interacting proteins and membranes.
- We will continue to focus on structural determination of supercomplex organization within the patient and control cell mitochondria.

III. Determine whether the respective mitochondrial disease-causing mutations alter the 3D structures of the mitochondrial respiratory complexes *in situ.*

- We will continue developing our computational pipelines to enable accurate particle-picking and subtomogram extraction to better resolve the respiratory complex structures directly affected by disease-causing mutations. Such automated, reference-free approaches as we are developing will ultimately replace laborious manual particle-picking and eliminate potential bias by human pickers. Additionally, as part of our collaborative efforts with Dr. Xu, we will further continue improving feature discrimination to optimize recognition of distinct protein confirmations/interactions by training an autoencoder model to denoise raw tomographic images and build a feature map featuring distortion-free enhanced images optimized for protein recognition. In parallel, we will continue optimizing the data acquisition parameters (*e.g.*, tilt schemes on the cryo-TEM microscope, total electron dose per tilt, use of a phase plate) to further improve the potential resolution of the complexes within the tomograms.

IV. Determine whether improved respiratory chain function in patient cells following treatment with JP4-039 is via the drug's ability to correct respiratory complex structural abnormalities.

- We will image patient and control fibroblasts with JP4-039 via *in situ* cryo-ET, to ascertain the effects of the drug directly on the 3D structures of the affected respiratory complexes at subnanometer resolution.

V. Visualize respiratory complex structure and supercomplex organization in healthy primary human fibroblasts after pesticide or pyridostigmine bromide treatment.

- Once we complete acquiring 3D tomographic data of patient and control human fibroblasts in the next 6-8 months, we will treat primary cells healthy controls with the pesticide paraquat. In parallel, we will treat these healthy control cells with the pesticide rotenone which specifically targets respiratory complex I. Use of the rotenone will allow us to compare and contrast paraquat's effects specifically on the structural organization of complex I as well as on higher order supercomplex organization. We will also treat a set of the control cells with pyridostigmine followed by their cryo-ET imaging. Finally, we plan on ascertaining whether these respective toxicant exposures produce structural differences different from those found in the patient cell lines both in terms of the individual respiratory complex 3D structures, as well as on the supercomplexes. In the event that the resolution is insufficiently high *in situ*, we will image purified mitochondria from treated cells to decrease background from the crowded cell environment and thus better resolve the affected complexes.

VI. Determine whether JP4-039 corrects mitochondrial structural abnormalities in GWI or pesticide and pyridostigmine-treated control cells.

- In the coming months, we will apply JP4-039 to our GWI samples as well as to healthy control fibroblasts pre-treated with either paraquat or pyridostigmine, followed by plunge-freezing and cryo-ET imaging. This will be followed by subtomogram averaging to determine whether JP4-039 improves the structural alterations evident in the respiratory complexes. We will then compare the respiratory complex structures in JP4-039-treated cells versus those treated with vehicle.

4. IMPACT

- **What was the impact on the development of the principal discipline(s) of the project?**
  Our results were disseminated to communities of interest at national and international scientific meetings. These meetings include the Annual Meeting of the American Society of Cell Biology (2020) and the Annual American Physical Society Meeting (2021). Additionally, results were presented as an invited speaker at Weill Cornell Medical College's Department of Biochemistry (2020). Collectively, presenting recent findings stemming from this project were instrumental in advancing the idea that *in situ* cryo-ET offers a new approach towards better understanding and treating mitochondrial diseases by identifying how these illnesses alter mitochondrial structure and morphology. This has begun generating considerable interest within the greater scientific community.

- **What was the impact on other disciplines?**
  In presenting results from this project, our findings were also broadly disseminated to a diverse scientific audience whose expertise spanned multiple disciplines including neuroscience, cell biology, microscopy, and clinical medicine. By appealing to a broader audience, this may foster in the longer-term new knowledge that leads to development of new, highly-targeted therapies for active military, Veterans, beneficiaries and the general population that are directed at correcting structural changes responsible for mitochondrial dysfunction. Ultimately, such a development could significantly reduce serious morbidity and mortality from mitochondrial diseases and its resulting neurological and cardiovascular consequences. Since current treatments only address disease symptoms, our project's development of methods to directly visualize mitochondrial disease-causing mutations and their effects on the mitochondrial architecture may produce new personalized interventions to treat underlying causes unique to each patient, significantly improving patient care for mitochondrial disorders. Such treatments may also boost mitochondrial function in healthy individuals and thus used as tools to increase fitness of active military personnel especially in combat situations. Moreover, this personalized approach to visualizing mitochondrial disorders can lead to fundamental insights into the mechanisms for development of these illnesses and may even be applied to the study of other diseases.

- **What was the impact on technology transfer?**
  Nothing to Report.

- **What was the impact on society beyond science and technology?**
  Nothing to Report.

5. CHANGES/PROBLEMS

There have been no changes in the scope of work since the last reporting periods and therefore the SOW remains the same as originally defined.

6. PRODUCTS

- **Publications, conference papers, and presentations**

Journal publications
Data based on the work resulting from this award has appeared in the following publications:

1. Zhu Y, Sun D, Schertel A, Ning J, Fu X, Guo P, Watson AM, **Freyberg Z**, Zhang P. Serial cryoFIB/SEM reveals profound cytoarchitectural disruptions caused by a pathogenic mutation in Leigh syndrome patient cells. Structure 2021. doi: 10.1016/j.str.2020.10.003. PubMed PMID: 33096015.

   We also have 3 manuscripts in preparation and expect to submit them in the next 6-12 months.

Books or other non-periodical, one-time publications
Nothing to report.

Other publications, conference papers, and presentations
Data based on the studies originally proposed for this award were presented at the following meetings and presentations:

1. Carter SD, Hampton CM, Langlois R, Melero R, Farino ZJ, Calderon MJ, Li W, Tran NH, Grassucci RA, Morgenstern TJ, Rice WJ, Wills ZP, Shiva S, Bartolini F, Murray SA, Aridor M, Fish KN, Walter P, Fass D, Wolf SG, Watkins SC, Carazo J, Jensen GJ, Frank J, **Freyberg Z**. (2020) Ribosome-Associated Vesicles: a dynamic sub-compartment of the endoplasmic reticulum in secretory cells. Abstract, poster and talk presented at the Cell Bio Virtual 2020 Annual Meeting of the American Society of Cell Biology, Virtual.

2. Carter SD, Hampton CM, Langlois R, Melero R, Farino ZJ, Calderon MJ, Li W, Tran NH, Grassucci RA, Morgenstern TJ, Rice WJ, Wills ZP, Shiva S, Bartolini F, Murray SA, Aridor M, Fish KN, Walter P, Fass D, Wolf SG, Watkins SC, Carazo J, Jensen GJ, Frank J, **Freyberg Z**. (2021) Opening a new window into the cell with super-resolution imaging and in situ cryo-electron tomography. Abstract and talk presented at the Annual Meeting of the American Physical Society, Virtual.

Additionally, Dr. Freyberg was an invited speaker at the following seminars where he presented the work produced from this funded work:

1. Invited speaker, Department of Biochemistry seminar series, Weill Cornell Medical College, Cornell University, New York, NY, Virtual; 2020
2. Invited speaker, Organelle Cross Talk and Contact Sites Symposium, Cell Bio Virtual 2020 Annual Meeting of the American Society of Cell Biology, Virtual; 2020
3. Invited speaker, American Physical Society Annual Meeting, Virtual; 2021

- **Website(s) or other Internet site(s)**

Nothing to Report.

- **Technologies or techniques**

Nothing to Report.

- **Inventions, patent applications, and/or licenses**

Nothing to Report.

- **Other Products**

Nothing to Report.

7. PARTICIPANTS & OTHER COLLABORATING ORGANIZATIONS

- **What individuals have worked on the project?**

• Name:	Zachary Freyberg M.D., Ph.D.
• Project Role:	Principal Investigator
• Researcher Identifier (*e.g.* ORCID ID):	ORCID ID: 0000-0001-6460-0118
• Nearest person month worked:	1.8
• Contribution to Project:	Dr. Freyberg has designed and analyzed all experimental data concerning both the live-imaging and *in situ* cryo-ET microscopy of mitochondria from cells taken from patients with mitochondrial disease and associated controls.
• Funding Support:	DoD Peer Reviewed Medical Research Program Discovery Award (PR192466); PA Tobacco Formula Fund, NIH/NIA R21 Award (R21AG068607), NIH NIDA CEBRA Award (R21DA052419), NIH/NIGMS R01 (R01GM134020), NIH/NIDDK R01 (R01DK109907), NIH/NHLBI/NIA R01 supplement (R01HL150432 Supplement)

• Name:	Jill Glausier, Ph.D.
• Project Role:	Co-Investigator
• Researcher Identifier (*e.g.* ORCID ID):	ORCID ID: 0000-0001-9838-3414
• Nearest person month worked:	0.6
• Contribution to Project:	Dr. Glausier has analyzed the tomographic data to successfully build three-dimensional maps of the imaged cells. She will use her expertise in mitochondrial assays to validate the structural findings concerning complex organization with biochemical assays on patient mitochondria including blue native gels and clinical electron transport chain analysis.
• Funding Support:	DoD Peer Reviewed Medical Research Program Investigator-Initiated Research (PR192466); NIH/NIDA (N0175N95019C00047), NIH/NIDA (DA051390)

• Name:	James Conway, Ph.D.
• Project Role:	Co-Investigator
• Researcher Identifier (*e.g.* ORCID ID):	ORCID ID: 0000-0002-6581-4748
• Nearest person month worked:	0.6
• Contribution to Project:	Dr. Conway has provided technical expertise and assistance with imaging and data analysis.

• Funding Support:	DoD Peer Reviewed Medical Research Program Investigator-Initiated Research (PR141292), NIH/NIAID (R01AI089803),

• Name:	Jiying Ning, Ph.D.
• Project Role:	Research Associate
• Researcher Identifier (*e.g.* ORCID ID):	N/A
• Nearest person month worked:	3.3
• Contribution to Project:	Dr. Ning has maintained the patient and control primary human cells (*e.g.*, primary fibroblasts) used in the study as well as optimized the sample preparation methodologies.
• Funding Support:	Department of Defense Peer Reviewed Medical Research Program Discovery Award (PR192466), PA Tobacco Formula Fund, NIH/NIGMS R01 (R01GM134020), NIH/NIDDK R01 (R01DK109907)

• Name:	Alexander Makhov, Ph.D.
• Project Role:	Facility Manager
• Researcher Identifier (*e.g.* ORCID ID):	N/A
• Nearest person month worked:	0.6
• Contribution to Project:	Dr. Makhov has assisted with data collection for the proposed cryo-electron microscopy and tomography data. He maintains the cryo-electron microscopes in an ongoing manner and conduct microscope repairs.
• Funding Support:	Department of Defense Peer Reviewed Medical Research Program Discovery Award (PR192466)

- **Has there been a change in the active other support of the PD/PI(s) or senior/key personnel since the last reporting period?**

Since the beginning of this project, the following is a change in the PI's active other support:

Grant Number (Funded)	Grant Title	Role in Project and Percentage of Effort	Years Inclusive	Source $ Amount (Total Costs)
PR192466	DoD Discovery Award, "A New *In Situ* Cryo-Electron Microscopy Approach to Directly Visualize Mutations in Mitochondrial Disease"	PI, 15% effort The goal of this award is to directly visualize mitochondrial disease in patient cells via *in situ* cryo-electron tomography	3/1/2020-2/28/2022	DoD (Direct:
PA-HEALT	PA Tobacco Formula Fund	PI, 20% effort The goal of this award is	6/1/2020-5/30/2024	PA State

	"Activity-Dependent Local Translation in Alzheimer's Disease"	to determine the role of the ER and mitochondria in activity-dependent local translation and the impact of Alzheimer's Disease on these processes		(Direct:
R21AG068607	Mechanisms for Preserving Neurons in Alzheimer's Disease-Related Dementias Across *Drosophila* and Mouse Models	PI, 15% effort The goal of this award is to determine whether dopamine neuron VGLUT expression is under tight regulatory control and if the genes involved are critical for VGLUT upregulation in synucleinopathy.	7/1/2020-6/30/2022	NIH/NIA (Direct:
R21DA052419	Ultra-fast high-resolution imaging of whole mouse brain for the study of drug addiction	MPI, 7.5% effort (Freyberg, Contact PI) This award will develop imaging and computational pipelines for high-throughput brain imaging in response to drugs of abuse.	3/1/2021-2/28/2023	NIH/NIDA (Direct:
R01GM134020	Novel Machine Learning Approaches for Improving Structural Discrimination in Cryo-Electron Tomography	Co-I, 9.1% effort (Min Xu, PI) The goal of this award is to develop novel computational pipelines for semi-automated approaches to analyze cryo-electron tomography data	6/10/2020-5/31/2024	NIH/NIGMS (Direct to ZF:
R01HL150432 Supplement	R01 "Cell-Type Specific Role of Circadian-Dependent Transcription in Fentanyl-Induced Synaptic and Behavioral Plasticity"	Co-I, 10% effort (Ryan Logan, PI) The goal of this award is to map different populations of neurons that are differentially activated in the context of opioid abuse in the whole brain.	8/1/2020-7/31/2021	NIH/NHLBI/NIA (Direct to ZF:
R01DK109907	R01 "Characterization of Branched Chain Amino Acid Metabolism and Its Deficiency"	Co-I, 20% effort (Gerard Vockley, PI) The long-range goal of this project is to characterize the metabolism of branched	3/1/2021-2/38/2026	NIH/NIDDK

		chain acyl-CoAs and to identify the consequences of its failure in humans.		

- **What other organizations were involved as partners?**

Nothing to Report.

8. SPECIAL REPORTING REQUIREMENTS

- **Collaborative Awards**

Not Applicable.

9. APPENDICES

We have included in the Appendix our recently published paper detailing the development and optimization of a serial cryoFIB/SEM volume imaging workflow for 3D visualization of entire patient cells from individuals with mitochondrial disorders. As proof of principle, we imaged through the complete depth of cells from people affected by Leigh syndrome.

Zhu Y, Sun D, Schertel A, Ning J, Fu X, Guo P, Watson AM, **Freyberg Z**, Zhang P. Serial cryoFIB/SEM reveals profound cytoarchitectural disruptions caused by a pathogenic mutation in Leigh syndrome patient cells. Structure 2021. doi: 10.1016/j.str.2020.10.003. PubMed PMID: 33096015.

Short Article

Structure

Serial cryoFIB/SEM Reveals Cytoarchitectural Disruptions in Leigh Syndrome Patient Cells

Graphical Abstract

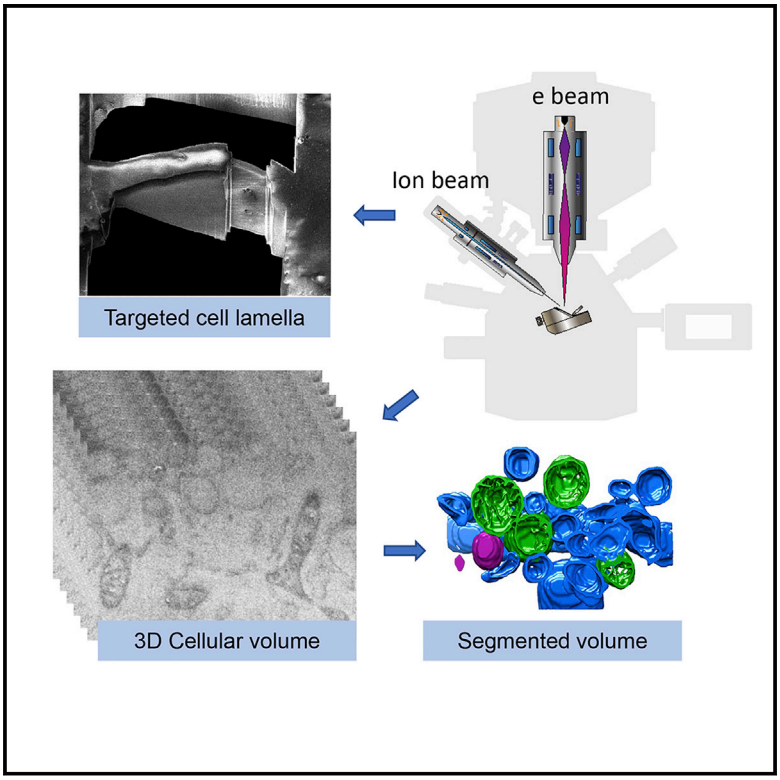

Authors

Yanan Zhu, Dapeng Sun, Andreas Schertel, ..., Marisa L. Martin-Fernandez, Zachary Freyberg, Peijun Zhang

Correspondence

peijun@strubi.ox.ac.uk

In Brief

Serial cryoFIB/SEM offers new opportunities for structural analysis of cells and tissues under near-native conditions. Zhu et al. developed and optimized a serial cryoFIB/SEM volume imaging workflow for visualization of entire vitreous cells in 3D, and demonstrated its potential for clinical and pathological applications with primary Leigh syndrome patient cells.

Highlights

- Developed and optimized a serial cryoFIB/SEM volume imaging workflow
- Visualized the 3D structure of an entire cell under native conditions
- Revealed a disruption of cellular structures in primary LS patient fibroblasts
- Demonstrated the potential for clinical phenotyping of pathogenic tissues

Zhu et al., 2021, Structure *29*, 82–87
January 7, 2021
https://doi.org/10.1016/j.str.2020.10.003

CellPress

CellPress
OPEN ACCESS

Structure

Short Article

Serial cryoFIB/SEM Reveals Cytoarchitectural Disruptions in Leigh Syndrome Patient Cells

Yanan Zhu,[1,8] Dapeng Sun,[2,8] Andreas Schertel,[3] Jiying Ning,[2] Xiaofeng Fu,[2] Pam Pam Gwo,[4] Alan M. Watson,[5] Laura C. Zanetti-Domingues,[6] Marisa L. Martin-Fernandez,[6] Zachary Freyberg,[4,5] and Peijun Zhang[1,2,7,9,*]

[1]Division of Structural Biology, Wellcome Trust Centre for Human Genetics, University of Oxford, Oxford OX3 7BN, UK
[2]Department of Structural Biology, University of Pittsburgh School of Medicine, Pittsburgh, PA 15260, USA
[3]Carl Zeiss Microscopy GmbH, Zeiss Customer Center Europe, Carl-Zeiss-Strassee 22, 73447 Oberkochen, Germany
[4]Department of Psychiatry, University of Pittsburgh, Pittsburgh, PA 15213, USA
[5]Department of Cell Biology, University of Pittsburgh, Pittsburgh, PA 15213, USA
[6]Central Laser Facility, Research Complex at Harwell, STFC Rutherford Appleton Laboratory, Harwell Oxford, Didcot, Oxford OX11 0QX, UK
[7]Electron Bio-Imaging Centre, Diamond Light Source, Harwell Science and Innovation Campus, Didcot OX11 0DE, UK
[8]These authors contributed equally
[9]Lead Contact
*Correspondence: peijun@strubi.ox.ac.uk
https://doi.org/10.1016/j.str.2020.10.003

SUMMARY

The advancement of serial cryoFIB/SEM offers an opportunity to study large volumes of near-native, fully hydrated frozen cells and tissues at voxel sizes of 10 nm and below. We explored this capability for pathologic characterization of vitrified human patient cells by developing and optimizing a serial cryoFIB/SEM volume imaging workflow. We demonstrate profound disruption of subcellular architecture in primary fibroblasts from a Leigh syndrome patient harboring a disease-causing mutation in USMG5 protein responsible for impaired mitochondrial energy production.

INTRODUCTION

Cryoelectron tomography (cryoET), with subtomogram averaging, has emerged as a powerful method for visualizing heterogeneous structures and *in situ* specimens at subnanometer resolutions (Himes and Zhang, 2018; Sutton et al., 2020; Zhang, 2019). However, due to limited penetrance of the electron beam in thicker regions of cells (Lucic et al., 2013; Wang et al., 2012), its utility is limited to very thin samples (<300 nm), such as thin regions of the cell periphery or cell lamella by cryo-focused ion beam (cryoFIB) thinning. On the other hand, serial FIB/scanning electron microscopy (SEM) has been rapidly adopted as a technique for generating large 3D volumes of cells and tissue constituents, which have been fixed (cryo or chemically), dehydrated, resin-embedded, and stained for imaging contrast (Kizilyaprak et al., 2019; Schirra and Zhang, 2014; Steyer et al., 2019). Its application to vitreous biological samples, namely serial cryoFIB/SEM, involves many challenges associated with low-contrast (no staining) and low-dose (radiation sensitive) imaging. Examples of serial cryoFIB/SEM showed its potential for studying whole-mount plunge-frozen and high-pressure frozen cells and tissues (Akiva et al., 2019; Schertel et al., 2013; Sviben et al., 2016; Vidavsky et al., 2015, 2016; Wu et al., 2020). We now explore this new capability for pathologic characterization of Leigh syndrome (LS) patient cells harboring a disease-causing mutation in USMG5 protein responsible for impaired mitochondrial energy production.

The primary role of mitochondria is to generate energy in cells through mitochondrial oxidative phosphorylation (OXPHOS) (Lake et al., 2015). OXPHOS deficiency leads to mitochondrial diseases, including LS, a devastating neurological disorder and the most common mitochondrial disease in children (Sofou et al., 2014). LS is genetically heterogeneous with more than 90 nuclear or mitochondrial genes implicated in its pathogenesis (Chang et al., 2020; McCormick et al., 2018). Virtually all of these genes encode the mitochondrial respiratory complex machinery required for energy generation through OXPHOS (Barca et al., 2018), including those regulating the structure and assembly of complex V (ATP synthase). Classical transmission electron microscopy of thin tissue sections from LS patients is typically used to diagnose mitochondrial disease, revealing abnormality of the structure of mitochondria (Lee et al., 2016). Disease-causing mutations, such as (T8993G-1) in cytochrome *c* oxidase (complex IV) and in SURF1 (a complex IV protein) were shown to lead to ultrastructural changes in mitochondria and, in the case of SURF1, also aggregation of abnormal intracellular inclusions (Makino et al., 2000; Pronicki et al., 2008). Recently a genetic study identified a novel pathogenic mutation (c.87 + 1G > C), in the *USMG5* gene that results in autosomal recessive LS (Barca et al., 2018). The mutation abolishes the canonical GT splice site donor of exon 4 of *USMG5* and produces aberrant transcripts that are degraded via nonsense-mediated decay with >90% loss of USMG5 expression (Barca et al., 2018). USMG5, also known as DAPIT (diabetes-associated protein in

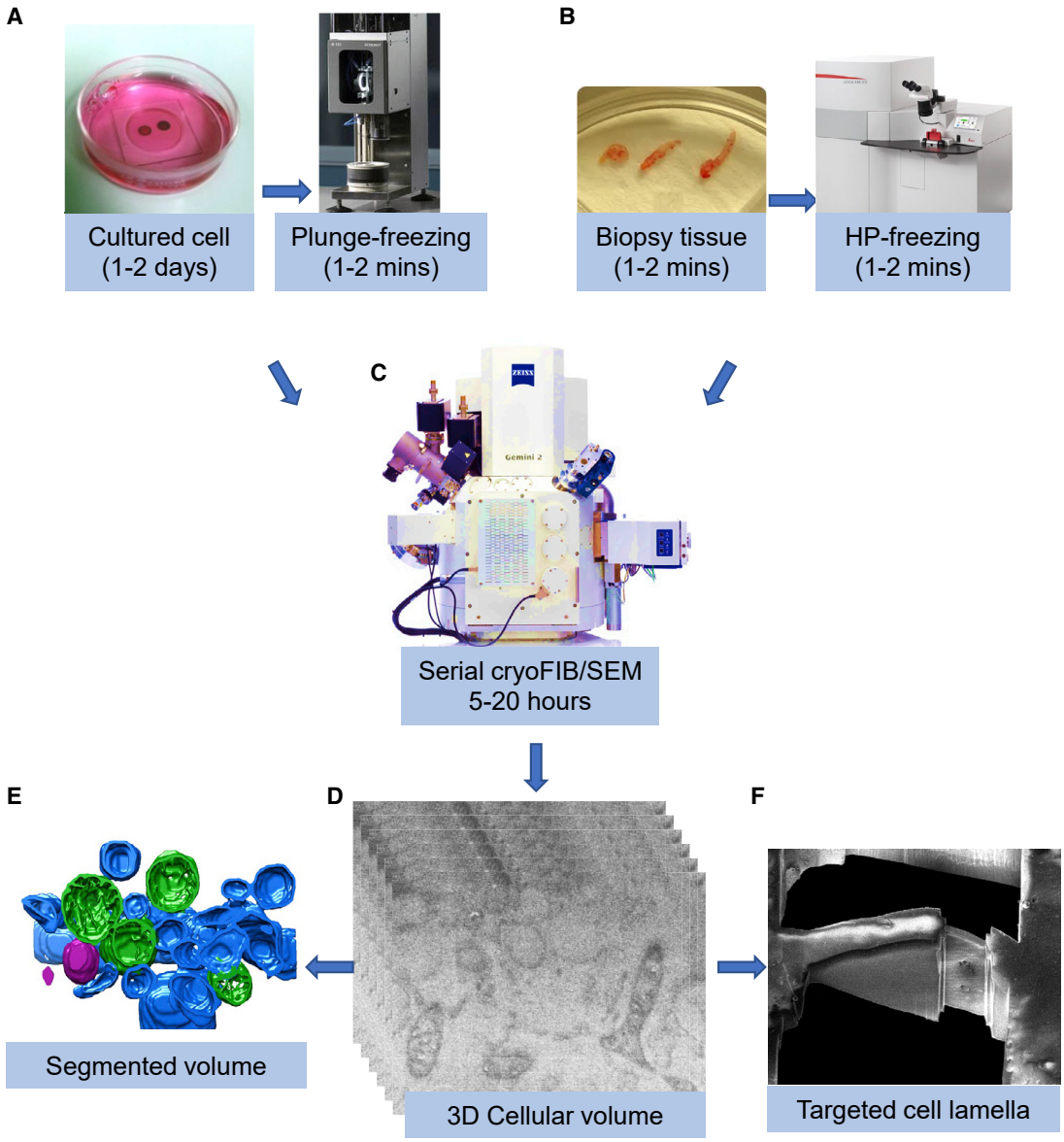

Figure 1. A Workflow for Serial cryoFIB/SEM Volume Imaging of Near-Native Cells and Tissues

(A) Cells cultured on EM grids are subjected to plunge freezing.

(B) Needle biopsy can be performed to extract tissues within 1–2 min, and immediately subjected to high pressure freezing.

(C) Serial cryoFIB/SEM is performed automatically for 5–20 h, depending on the volume to be imaged, dwell time, and average line count.

(D) A stack of 2D cryoSEM images enclosing the volume of the cell.

(E) 3D segmentation of the cell volume.

(F) Targeted cell lamella preparation on the intracellular region of interest identified by serial cryoFIB/SEM.

insulin-sensitive tissues), is a constituent of complex V required for its dimerization. Complex V ordinarily exists as a dimeric supercomplex required to shape the mitochondrial cristae, enabling efficient flow of the protons needed to fuel ATP synthesis. Recent cryoET of thin peripheral regions of LS patient cells harboring this *USMG5* gene mutation revealed significant disturbances in mitochondrial crista (Siegmund et al., 2018). The effect of the *USMG5* mutation on the level of whole-cell and subcellular architecture, however, has not been investigated.

Here, we developed and optimized a workflow using serial cryoFIB/SEM to study whole plunge-frozen primary fibroblast cells from a healthy individual and from an LS patient carrying the homozygous mutation in the *USMG5* gene previously shown to impair mitochondria cristae structure and ATP synthesis (Siegmund et al., 2018). The resulting 3D volumes of patient and control cells demonstrate a profound disruption of cellular and subcellular structures in LS patient cells. Compared with conventional serial FIB/SEM of stained and resin-embedded samples, serial cryoFIB/SEM offers a much faster (without a

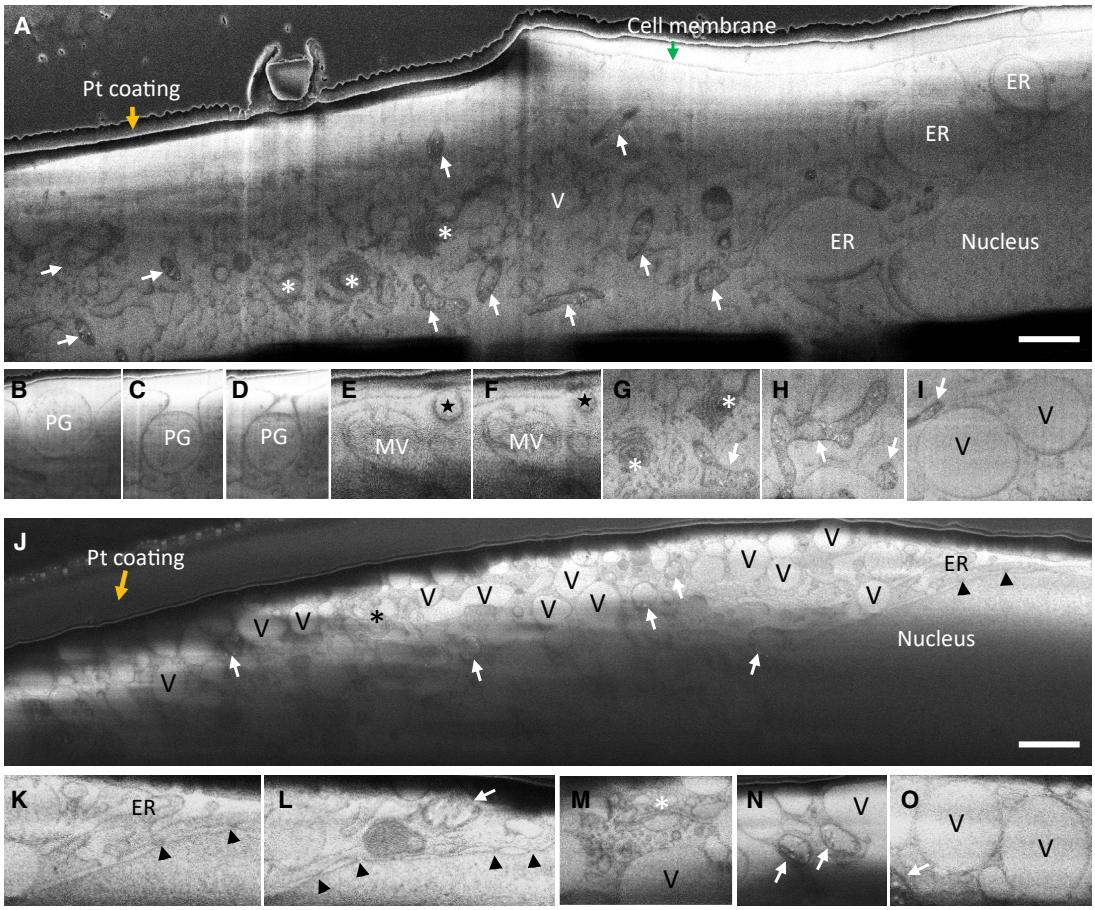

Figure 2. Serial cryoFIB/SEM of Frozen-Hydrated Primary Cells from Control and Patient Fibroblasts

(A) A representative cryoSEM image from a stack of 575 serial micrographs recorded from a control fibroblast cell cultured on an EM grid.

(B–I) An image gallery of subcellular structures and organelles observed in the control cell, including three consecutive slices of a phagosome entering the cell (B–D), two consecutive slices of an endosome (E and F, star), a multivesicular body (E and F, MV), Golgi complexes (G, asterisks), tubular-shaped mitochondria (G and H, arrow), and vacuoles (I and V).

(J) A representative cryoSEM image from a stack of 2018 serial micrographs recorded from a patient fibroblast cell cultured on an EM grid.

(K–O) An image gallery of subcellular structures and organelles observed in the patient cell, showing endoplasmic reticulum (K, ER), nuclear pores (K and L, arrowheads), Golgi complex (M, asterisk), mitochondria (L and N, arrows), and vacuoles (M, O, and V). Arrows, mitochondria; asterisks, Golgi; stars, endosome; PG, phagosome; MV, multivesicular body; V, vacuoles; arrowheads, nuclear pore; orange arrows, platinum GIS coating; green arrow, cell membrane; ER, endoplasmic reticulum. Scale bars, 1 μm.

lengthy dehydration and embedding process during sample preparation) and close-to-native technique for phenotypic characterization of whole cells or tissue, which could be exceedingly useful in clinical settings.

RESULTS

A Workflow for 3D Volume Imaging of Near-Native Cells and Tissues

To investigate the phenotypic impact of a specific *USMG5* gene mutation (c.87 + 1G > C) on cellular and subcellular structures in a near-native state, we cultured the primary fibroblast cells isolated from an LS patient and from a healthy individual on gold EM grids, which were subsequently plunge-frozen (Figure 1). Serial cryoFIB sectioning and cryoSEM imaging of frozen-hydrated primary fibroblast cells were performed using a Zeiss Cross-beam 550 instrument (Table S1). To maximize the cryoSEM image contrast and balance between resolution and total volume and time, we tested a number of FIB and SEM parameters, including pixel spacing, FIB slice thickness, FIB and SEM probe currents, acceleration potential, SEM dwell time, and average line count. Using a lateral pixel spacing of 10.5 nm for SEM imaging and a FIB slice thickness of 21.0 nm, an entire patient fibroblast cell was sliced through and 2018 slices were imaged at 4,096 × 3,072 pixels in about ~17.5 h, resulting in a total volume of 58,789 μm^3 (Video S1). For the control fibroblast cell, a similar voxel size was used, but a reduced raster of 3,072 × 1,150 pixels was used for imaging in total 575 slices. A total volume of 4,062 μm^3 was obtained within ~5.5 h for the control cell (Video S2). Detailed parameters are listed in Table S1. The density profile plots indicate that the resolution of cryoSEM images is at least 37 nm with 10 nm pixel size under the image conditions

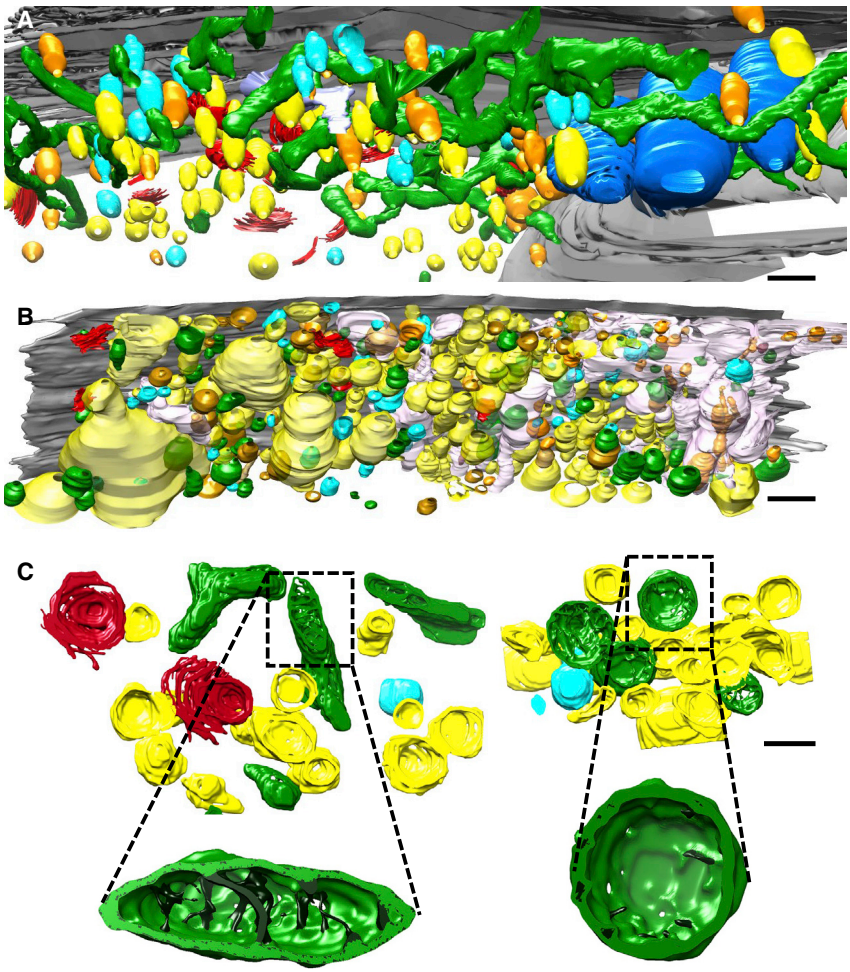

Figure 3. 3D Reconstruction and Segmentation of Control and Patient Cells

(A and B) Surface rendering of segmented volumes of control (A) and patient (B) fibroblast cells. Green, mitochondria; red, Golgi, yellow, vacuoles; orange, dense vesicles; cyan, partially dense vesicles; blue, ER.

(C) Segmentation of a small representative volume from control (left) and patient (right) fibroblasts. Inserts are enlarged views of a single mitochondrion in control (left) and patient (right) cells. Cristae are shown in dark green. Scale bars, 1 μm (A and B) and 500 nm (C).

specified (Figure S1). The actual resolution might be assessed using a crystalline material.

Serial cryoFIB/SEM Volume Imaging of Control and Patient Fibroblasts

Figure 2 shows cryoSEM images of representative slices from both patient and control cells. We noted a contrast imbalance between the lower part and the upper part of the cross-sectioned patient cell (Figure 2J). Since the cryoSEM image contrast is related to local surface potentials, the median potential (or threshold) can be different depending on the environment and local charge dissipation, such as the top cell region being close to the cold deposited platinum precursor layer and bottom part being in the vicinity of the support film and grid bars. In both cells, subcellular structures are clearly visible, especially membrane-enclosed subcellular compartments (Figures 2A and 2J), including the nucleus. Notably, serial cryoFIB/SEM provides unambiguous visualization of nuclear pores in human cells (Figures 2J–2L, arrowheads), which had not been achieved previously using this method. In the control cell, individual cellular organelles can be identified based on their distinct morphologies, including the cell membrane, a phagosome (Figures 2B–2D, PG, in three consecutive slices), endoplasmic reticulum, multivesicular bodies (Figures 2E and 2F, MV), Golgi (Figure 2G, *), mitochondria (Figures 2G–2I, white arrows), vacuole-like membranous structures (Figures 2I and 2V), and the cell nucleus. The LS patient fibroblast cell, however, shows substantial cytoarchitectural derangements, with the interior of the cell largely occupied by vacuolated structures of indeterminate origin. Of the residual identifiable structures, including mitochondria and Golgi, organelles are significantly decreased in volume and displayed gross morphological abnormalities. For example, the Golgi apparatus lacks extended membrane stacks (Figures 2J and 2M). More remarkably, compared with the complex shape and network of mitochondria in the control cell (Figures 2A, 2G, and 2H; Video S2), nearly all patient mitochondria are roughly round with minimal cristae (Figures 2J, 2L, and 2N; Video S1), consistent with our previous cryoET analyses (Siegmund et al., 2018). This suggests that the architecture responsible for energy metabolism in the patient cells is compromised, consistent with the earlier biochemical characterization of these primary fibroblasts (Barca et al., 2018). The patient cells also grow substantially slower than the control cells.

3D Reconstruction and Segmentation of Control and Patient Cells

For further analysis, we have performed 3D reconstruction and segmentation of the serial cryoFIB/SEM volume data for both patient and control cells (Figures 3A and 3B; Videos S1 and S2). In the volume rendering of the control cell, an extended network of oblate tubular-shaped mitochondria is evident (Figure 3A, green; Video S3), whereas the patient cell shows mitochondria that are discrete and mostly round or oval-shaped individuals (Figure 3B, green; Video S4). Some individual mitochondria appear in close association with one another in both control and patient cells (Figure S2). The size of vacuoles (Figure 3B, yellow) within the patient cell are also remarkably larger than those of the control cell, more abundant and densely packed (Figures 2A, 2J, 3A, and 3B). The overall volume of mitochondria and number of each organelle in patient and control cells are compared in Figure S3. To analyze the structural details of organelles, a small region of the cell was cropped and

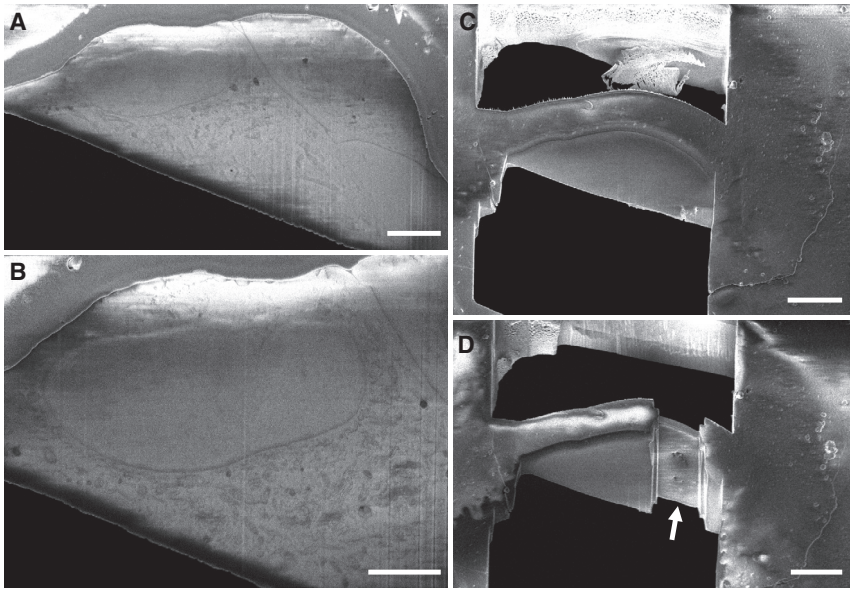

Figure 4. Targeted Cell Lamella Preparation by Serial cryoFIB/SEM

(A and B) Two representative cryoSEM images of cryoFIB block face, 320 nm apart.

(C and D) CryoSEM images of cell lamella preparation at the same region shown in (B). Arrow points to the thin lamella. Scale bars, 5 μm (A and B) and 10 μm (C and D).

segmented semi-automatically, as shown in Figures 3C and 3D (Videos S5 and S6). We can appreciate the drastic differences in the morphology of mitochondria and the shape and distribution of cristae between patient and control cells. Cristae structure is severely disturbed in the patient cell, appearing sparse in number and short, as previously observed by cryoET of limited regions of the cell periphery (Siegmund et al., 2018). The dramatic impact of complex V's failure to dimerize due to a specific *USMG5* gene mutation on overall cellular architecture and organelle structures in LS patient cells is now more fully appreciated in the greater context of the whole cell through *in situ* large volume imaging.

DISCUSSION

The majority of imaging studies on LS disease have been understandably focused on mitochondria. Nevertheless, our work demonstrates dramatic phenotypic changes to LS patient cells that extend beyond mitochondria to alter most, if not all, organelles within the cell, in particular a substantial accumulation of vacuoles. This is consistent with a recent study with PARL-deficient (*Parl*$^{-/-}$) mice exhibiting a Leigh-like syndrome, where, in addition to mitochondrial structural changes, similar intracellular vacuolization was observed in a response to alterations in complex III (Spinazzi et al., 2019). Using emerging serial cryoFIB/SEM technology, we captured and visualized an entire frozen-hydrated mammalian cell in 3D. More importantly, we applied this capability to studies of human disease cellular processes. This revealed a profound disruption of cellular and subcellular structures in a primary LS patient fibroblast cells. Such whole-cell volume phenotypic characterization of cells and tissues *in situ*, at the near-native state, offers an opportunity to improve our understanding of diseases beyond LS and potentially provides new means for clinical use, from diagnosis to treatment. The potential of combining large-scale cryo-volume imaging using serial cryoFIB/SEM, followed by cryoFIB lamella preparation of the specific region of interest identified through serial cryoFIB/SEM (Figure 4), with cryoET imaging of the targeted lamella at a high resolution on the exact same object, is especially exciting.

STAR★METHODS

Detailed methods are provided in the online version of this paper and include the following:

- KEY RESOURCES TABLE
- RESOURCE AVAILABILITY
  - Lead Contact
  - Materials Availability
  - Data and Code Availability
- EXPERIMENTAL MODEL AND SUBJECT DETAILS
  - Ethics Statement
  - Cell Lines
  - Primary Cell Cultures
- METHODS DETAILS
  - Sample Preparation
  - Serial cryoFIB/SEM
  - Local Reconstruction and Subvolume Segmentation
  - Global Image Alignment and 3D Modelling
- QUANTIFICATION AND STATISTICAL ANALYSIS

SUPPLEMENTAL INFORMATION

Supplemental Information can be found online at https://doi.org/10.1016/j.str.2020.10.003.

ACKNOWLEDGMENTS

We thank Drs. Teresa Brosenitsch and Luiza Mendonça for critical reading of the manuscript. We are grateful to Dr. Michio Hirano for providing the control and patient cells. We also thank Drs. James Gilchrist for technical support, and Drs. Tao Ni, Min Xu, Julika Radecke, and Andrew Howe for helpful discussions about segmentation. We thank Dr. Saskia Mimietz-Oeckler and Andreas Halladay, Leica Microsystems, for technical support. This work was supported by

the Department of Defense grants PR141292 (to Z.F.) and PR192466 (to Z.F.), the NIH P50 grant AI150481 (to P.Z.), the UK Wellcome Trust Investigator Award 206422/Z/17/Z (to P.Z.), and the UK Biotechnology and Biological Sciences Research Council grant BB/S003339/1 (to P.Z.).

AUTHOR CONTRIBUTIONS

P.Z. conceived and designed the experiments. J.N. cultured cells and X.F. prepared cryo-specimens. A.S., L.C.Z.-D., and M.L.M.-F. performed serial cryo-FIB/SEM. Y.Z., P.P.G., A.M.W., and D.S. performed segmentation and, with P.Z., analyzed data. Y.Z. and P.Z. wrote the paper with support from other authors.

DECLARATION OF INTERESTS

The authors declare no competing interests.

Received: June 26, 2020
Revised: August 31, 2020
Accepted: October 5, 2020
Published: October 22, 2020

REFERENCES

Akiva, A., Nelkenbaum, O., Schertel, A., Yaniv, K., Weiner, S., and Addadi, L. (2019). Intercellular pathways from the vasculature to the forming bone in the zebrafish larval caudal fin: possible role in bone formation. J. Struct. Biol. *206*, 139–148.

Barca, E., Ganetzky, R.D., Potluri, P., Juanola-Falgarona, M., Gai, X., Li, D., Jalas, C., Hirsch, Y., Emmanuele, V., Tadesse, S., et al. (2018). USMG5 Ashkenazi Jewish founder mutation impairs mitochondrial complex V dimerization and ATP synthesis. Hum. Mol. Genet. *27*, 3305–3312.

Cardona, A., Saalfeld, S., Schindelin, J., Arganda-Carreras, I., Preibisch, S., Longair, M., Tomancak, P., Hartenstein, V., and Douglas, R.J. (2012). TrakEM2 software for neural circuit reconstruction. PLoS One *7*, e38011.

Chang, X., Wu, Y., Zhou, J., Meng, H., Zhang, W., and Guo, J. (2020). A meta-analysis and systematic review of Leigh syndrome: clinical manifestations, respiratory chain enzyme complex deficiency, and gene mutations. Medicine (Baltimore) *99*, e18634.

Himes, B.A., and Zhang, P. (2018). emClarity: software for high-resolution cryo-electron tomography and subtomogram averaging. Nat. Methods *15*, 955–961.

Kremer, J.R., Mastronarde, D.N., and McIntosh, J.R. (1996). Computer visualization of three-dimensional image data using IMOD. J. Struct. Biol. *116*, 71–76.

Kizilyaprak, C., Stierhof, Y.D., and Humbel, B.M. (2019). Volume microscopy in biology: FIB-SEM tomography. Tissue Cell *57*, 123–128.

Lake, N.J., Bird, M.J., Isohanni, P., and Paetau, A. (2015). Leigh syndrome: neuropathology and pathogenesis. J. Neuropathol. Exp. Neurol. *74*, 482–492.

Lee, J.S., Kim, H., Lim, B.C., Hwang, H., Choi, J., Kim, K.J., Hwang, Y.S., and Chae, J.H. (2016). Leigh syndrome in childhood: neurologic progression and functional outcome. J. Clin. Neurol. *12*, 181–187.

Lowe, D.G. (2004). Distinctive image features from scale-invariant keypoints. Int. J. Comput. Vis. *60*, 91–110.

Lucic, V., Rigort, A., and Baumeister, W. (2013). Cryo-electron tomography: the challenge of doing structural biology in situ. J. Cell Biol. *202*, 407–419.

Makino, M., Horai, S., Goto, Y., and Nonaka, I. (2000). Mitochondrial DNA mutations in Leigh syndrome and their phylogenetic implications. J. Hum. Genet. *45*, 69–75.

McCormick, E.M., Zolkipli-Cunningham, Z., and Falk, M.J. (2018). Mitochondrial disease genetics update: recent insights into the molecular diagnosis and expanding phenotype of primary mitochondrial disease. Curr. Opin. Pediatr. *30*, 714–724.

Pettersen, E.F., Goddard, T.D., Huang, C.C., Couch, G.S., Greenblatt, D.M., Meng, E.C., and Ferrin, T.E. (2004). UCSF Chimera—a visualization system for exploratory research and analysis. J. Comput. Chem. *25*, 1605–1612.

Pronicki, M., Matyja, E., Piekutowska-Abramczuk, D., Szymanska-Debinska, T., Karkucinska-Wieckowska, A., Karczmarewicz, E., Grajkowska, W., Kmiec, T., Popowska, E., and Sykut-Cegielska, J. (2008). Light and electron microscopy characteristics of the muscle of patients with SURF1 gene mutations associated with Leigh disease. J. Clin. Pathol. *61*, 460–466.

Schertel, A., Snaidero, N., Han, H.M., Ruhwedel, T., Laue, M., Grabenbauer, M., and Mobius, W. (2013). Cryo FIB-SEM: volume imaging of cellular ultrastructure in native frozen specimens. J. Struct. Biol. *184*, 355–360.

Schirra, R.T., Jr., and Zhang, P. (2014). Correlative fluorescence and electron microscopy. Curr. Protoc. Cytom. *70*, 12 36 11–10.

Siegmund, S.E., Grassucci, R., Carter, S.D., Barca, E., Farino, Z.J., Juanola-Falgarona, M., Zhang, P.J., Tanji, K., Hirano, M., Schon, E.A., et al. (2018). Three-dimensional analysis of mitochondrial crista ultrastructure in a patient with Leigh syndrome by in situ cryoelectron tomography. Iscience *6*, 83.

Sofou, K., De Coo, I.F., Isohanni, P., Ostergaard, E., Naess, K., De Meirleir, L., Tzoulis, C., Uusimaa, J., De Angst, I.B., Lonnqvist, T., et al. (2014). A multicenter study on Leigh syndrome: disease course and predictors of survival. Orphanet J. Rare Dis. *9*, 52.

Spinazzi, M., Radaelli, E., Horre, K., Arranz, A.M., Gounko, N.V., Agostinis, P., Maia, T.M., Impens, F., Morais, V.A., Lopez-Lluch, G., et al. (2019). PARL deficiency in mouse causes complex III defects, coenzyme Q depletion, and Leigh-like syndrome. Proc. Natl. Acad. Sci. U S A *116*, 277–286.

Steyer, A.M., Schertel, A., Nardis, C., and Mobius, W. (2019). FIB-SEM of mouse nervous tissue: fast and slow sample preparation. Methods Cell Biol. *152*, 1–21.

Sutton, G., Sun, D., Fu, X., Kotecha, A., Hecksel, C.W., Clare, D.K., Zhang, P., Stuart, D.I., and Boyce, M. (2020). Assembly intermediates of orthoreovirus captured in the cell. BioRxiv. https://doi.org/10.1101/2020.06.10.144998.

Sviben, S., Gal, A., Hood, M.A., Bertinetti, L., Politi, Y., Bennet, M., Krishnamoorthy, P., Schertel, A., Wirth, R., Sorrentino, A., et al. (2016). A vacuole-like compartment concentrates a disordered calcium phase in a key coccolithophorid alga. Nat. Commun. *7*, 11228.

Vidavsky, N., Addadi, S., Schertel, A., Ben-Ezra, D., Shpigel, M., Addadi, L., and Weiner, S. (2016). Calcium transport into the cells of the sea urchin larva in relation to spicule formation. Proc. Natl. Acad. Sci. U S A *113*, 12637–12642.

Vidavsky, N., Masic, A., Schertel, A., Weiner, S., and Addadi, L. (2015). Mineral-bearing vesicle transport in sea urchin embryos. J. Struct. Biol. *192*, 358–365.

Wang, K., Strunk, K., Zhao, G., Gray, J.L., and Zhang, P. (2012). 3D structure determination of native mammalian cells using cryo-FIB and cryo-electron tomography. J. Struct. Biol. *180*, 318–326.

Wu, G.H., Mitchell, P.G., Galaz-Montoya, J.G., Hecksel, C.W., Sontag, E.M., Gangadharan, V., Marshman, J., Mankus, D., Bisher, M.E., Lytton-Jean, A.K.R., et al. (2020). Multi-scale 3D cryo-correlative microscopy for vitrified cells. Structure. https://doi.org/10.1016/j.str.2020.07.017.

Zhang, P. (2019). Advances in cryo-electron tomography and subtomogram averaging and classification. Curr. Opin. Struct. Biol. *58*, 249–258.

STAR★METHODS

KEY RESOURCES TABLE

REAGENT or RESOURCE	SOURCE	IDENTIFIER
Biological Samples		
Fetal bovine serum	Sigma-Aldrich	12103C
Chemicals, Peptides, and Recombinant Proteins		
MEM Vitamin solution	Thermo Fisher	11120037
Antibiotic-antimycotic	Thermo Fisher	15240062
Dulbecco's minimal essential media (DMEM)	Thermo Fisher	11965092
Fibronectin	Sigma-Aldrich	33016015
Deposited Data		
Serial cryoFIB/SEM raw images	This Paper	EMPIAR-10515
Experimental Models: Cell Lines		
Primary skin fibroblasts from a patient carrying a homozygous USMG5 mutation (C.87+1G>C, 1 base pair after the end of Exon 3)	Siegmund et al., 2018	N/A
Primary control cells from healthy human subjects	Siegmund et al., 2018	N/A
Software and Algorithms		
IMOD	Kremer et al., 1996	https://bio3d.colorado.edu/imod/
MATLAB	MathWorks	https://www.mathworks.com/products/matlab.html
Chimera	Pettersen et al., 2004	https://www.cgl.ucsf.edu/chimera/
TrakEM2	Cardona et al., 2012	https://imagej.net/TrakEM2
Other		
Quantifoil Gold R2/2 grids, 300 mesh	Quantifoil	Q350AR2
Glass-bottom culture dishes	MatTek Corporation	P35G-1.5-7-C

RESOURCE AVAILABILITY

Lead Contact

Further information and requests should be directed and will be fulfilled by the Lead Contact, Prof. Peijun Zhang, (peijun@strubi.ox.ac.uk).

Materials Availability

This study did not generate new unique reagents.

Data and Code Availability

The raw Serial cryoFIB/SEM images during this study has been deposited at EMPIAR (https://www.ebi.ac.uk/pdbe/emdb/empiar/) with the access code EMPIAR-10515.

EXPERIMENTAL MODEL AND SUBJECT DETAILS

Ethics Statement

The research received approval from the MRC Regulatory Support Centre.

Cell Lines

Skin fibroblasts from a patient carrying a homozygous USMG5 mutation (C.87+1G>C, 1 base pair after the end of Exon 3), and control cells from both male and female healthy human subjects are provided by Dr. Michio Hirano, Columbia University. Cell lines have not been authenticated.

Primary Cell Cultures

Cells were cultured in Dulbecco's minimal essential media (DMEM) (Thermo Fisher, Waltham, MA, USA) supplemented with 15% fetal bovine serum (FBS) (Sigma-Aldrich, St. Louis, MO, USA), 1% vitamin solution and 1% antibiotic-antimycotic (Thermo Fisher) as described earlier(Siegmund et al., 2018).

METHODS DETAILS

Sample Preparation

All experiments were conducted on cells cultured for <15 passages. Cells were plated onto gold R2/2 Quantifoil finder EM grids (Quantifoil Micro Tools GmbH, Jena, Germany) at density of 0.5-1 × 10^5 cells/ml (total 2 ml culture) in glass-bottom culture dishes (MatTek Corporation, Ashland, MA). The gold EM grids were coated with 50 μg/ml fibronectin (Sigma-Aldrich) and sterilized under UV light for 2 hours before use. For the control cells, after 48 hours culture, the grids were blotted with a filter paper and plunge-frozen into liquid ethane for rapid vitrification using an FEI Vitrobot (FEI, Hillsboro, OR) at ~100% humidity. Patient cells grew slowly and were cultured for 5 days before plunge-freezing.

Serial cryoFIB/SEM

For patient cells, the plunge-frozen EM grid was mounted in a Leica Vacuum Cryo Manipulation (VCM) preparation box (Leica Microsystems GmbH, Vienna, Austria) on a Leica cryo-holder for freeze-fracturing under cryogenic conditions. The TEM grid was held down on the flat top surface by using the clamp. The sample holder was transferred into a Leica ACE 600 cryo-sputter coater using a Leica VCT500 sample shuttle (Leica Microsystems, Vienna, Austria). At -154°C, the sample was sputter-coated with a 4 nm thick tungsten layer. The samples were then transferred into a ZEISS Crossbeam 550 FIB-SEM (Carl Zeiss Microscopy GmbH, Oberkochen, Germany). The cryo-stage temperature was maintained at -155°C and the system vacuum was 1.6×10^{-6} mbar. For areas containing cells, a cold deposition of platinum precursor material was achieved by opening the gas valve for 45 seconds. For cold deposition, the gas reservoir temperature was 28°C, and the distance between the gas capillary and the sample was about 3 mm.

First, a viewing channel for SEM imaging was milled using a FIB-milling probe current of 7 nA. The resulting cross-section was polished with a FIB probe current of 3 nA. For serial sectioning and imaging, a FIB probe current of 700 pA was used, and the FIB slice thickness was 21 nm. SEM images using InLens SE detection with a SEM probe current of 35 pA, a SEM acceleration potential of 2.3 keV and a dwell time of 100 ns were recorded. The lateral pixel spacing for SEM imaging was 10.5 nm and the image size was 4096 × 3072 pixels. Line Average with a line average count N = 61 was used for noise reduction.

The control cell sample (bare-TEM grid clipped into an autogrid ring) was mounted on a pre-tilted Leica sample holder for on-grid-thinning (Leica Microsystems GmbH, Vienna, Austria). After sputter-coating and transfer into the Crossbeam 550 FIB/SEM, a cold deposition of platinum precursor was done following the same procedure as above. The Crossbeam 550 system pressure was 8×10^{-7} mbar. A FIB probe current of 700 pA and a FIB slice thickness of 20 nm were used for serial sectioning and imaging. The lateral pixel spacing for SEM imaging was 10 nm and the imaging box was reduced to 3072 × 1150 pixel since the cell width is much larger than its height. For SEM imaging, InLens SE detection, a SEM probe current of 59 pA, a SEM acceleration potential of 1.9 keV and a dwell time of 200 ns were used. We employed a line average count N = 19 was used for noise reduction.

For cryoSEM imaging, the acceleration potential influences sample charging and is chosen in order to minimize sample charging and charging artefacts at interfaces. Due to the different mounting geometry, sample charging conditions are affected, and the acceleration potential is varied to optimize for imaging conditions. Since a charging and beam sensitive sample is imaged, short dwell times are advantageous and the total electron dose (beam current * dwell time * line average count) is restricted to minimize beam damage. By variation of how a specific electron dose is provided the imaging conditions are optimized especially near interfaces.

Local Reconstruction and Subvolume Segmentation

The raw SEM images were first aligned and a 3D volume generated using IMOD(Kremer et al., 1996). Subvolumes with representative features were cropped out from each aligned image stack (300×200 pixel × 40 slices or ~3.2 × 2.1 × 0.84 μm for patient cell and 500×400 pixel×40 slices or ~5.0 × 4.0 × 0.8 μm for control cell). The alignment between images was refined using an in-house Matlab script based on the Imregister function. To make objects smooth, 19 additional images were generated, with a linear interpolation, and inserted between two successive image slices with a home-made Matlab script. Using PixelAnnotationTool available online (https://github.com/abreheret/PixelAnnotationTool/releases), specific organelles, such as mitochondria, Golgi etc., were labeled manually from the cropped images as masks, which were then used to extract the image data from the corresponding region separately. These segmented image volumes were displayed in Chimera(Pettersen et al., 2004).

Global Image Alignment and 3D Modelling

The region containing the cell content was masked using Chimera software(Pettersen et al., 2004) with a boundary contour that was generated in 3dmod to just include the cell. The masked image slices (237 slices from the control cell and 218 slices from the patient cell) were first aligned with the Tiltxcorr(Kremer et al., 1996) program in IMOD using cross-correlation to determine the X and Y translations between successive image slices. The coarse-aligned image stacks were registered further using a SIFT-based

algorithm(Lowe, 2004) adapted to run on TrakEM2 plugin for FIJI(Cardona et al., 2012). The post-registration images were exported into 3dmod(Kremer et al., 1996) for further manual segmentation. Chimera was used for display of segmented 3D models.

QUANTIFICATION AND STATISTICAL ANALYSIS

The parameters of serial cryoFIB/SEM in Table S1 are optimal imaging conditions. Resolution assessment was done through density profile plot in Digital Micrograph (Gatan Inc.) software and presented in Figure S1. The numbers for specific organelles were counted from the segmented cells and presented in Figure S3. The volumes for segmented mitochondria were calculated in IMOD and presented in Figure S3.

Structure, Volume *29*

Supplemental Information

Serial cryoFIB/SEM Reveals Cytoarchitectural Disruptions in Leigh Syndrome Patient Cells

Yanan Zhu, Dapeng Sun, Andreas Schertel, Jiying Ning, Xiaofeng Fu, Pam Pam Gwo, Alan M. Watson, Laura C. Zanetti-Domingues, Marisa L. Martin-Fernandez, Zachary Freyberg, and Peijun Zhang

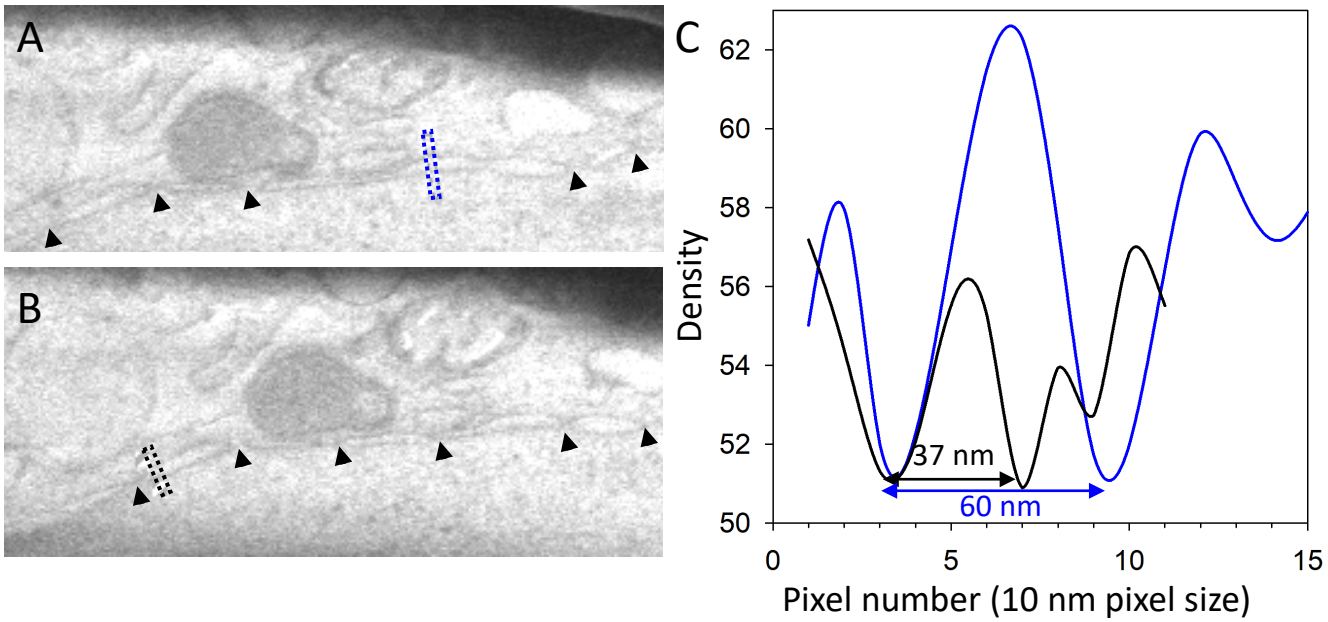

Figure S1 | Resolution assessment. A-B) Representative cryoSEM images from a stack of 2018 serial micrographs recorded from a patient fibroblast cell. Black arrow heads indicate nuclear pores. Blue and black boxes enclose areas for density profile. C) Density profile plots of the nuclear membranes. The blue line from the area shown in (A) and the black line from the area shown in (B). The separation between the two membranes is 37 nm in (B). Related to Figure 2.

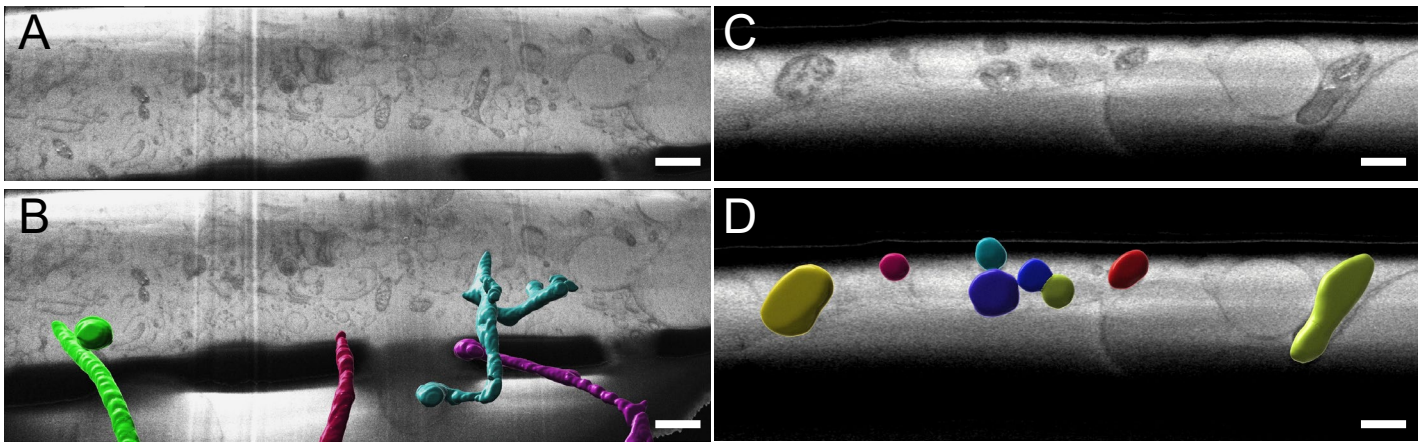

Figure S2 | Close association of mitochondria in control (A-B) and patient (C-D) cells. Mitochondria were manually segmented from control (A) and patient (C) datasets using NIS Elements (Nikon). The segmented images were overlaid with the RAW data in Imaris 9.5 (Bitplane) where the segmented areas were transformed into objects using surfacing tools (B and D, also see Movie S7 and S8). Independent objects are signified by a unique color. Scale bars, 1 µm in a & b, 0.3 µm in C & D. Related to Figure 3.

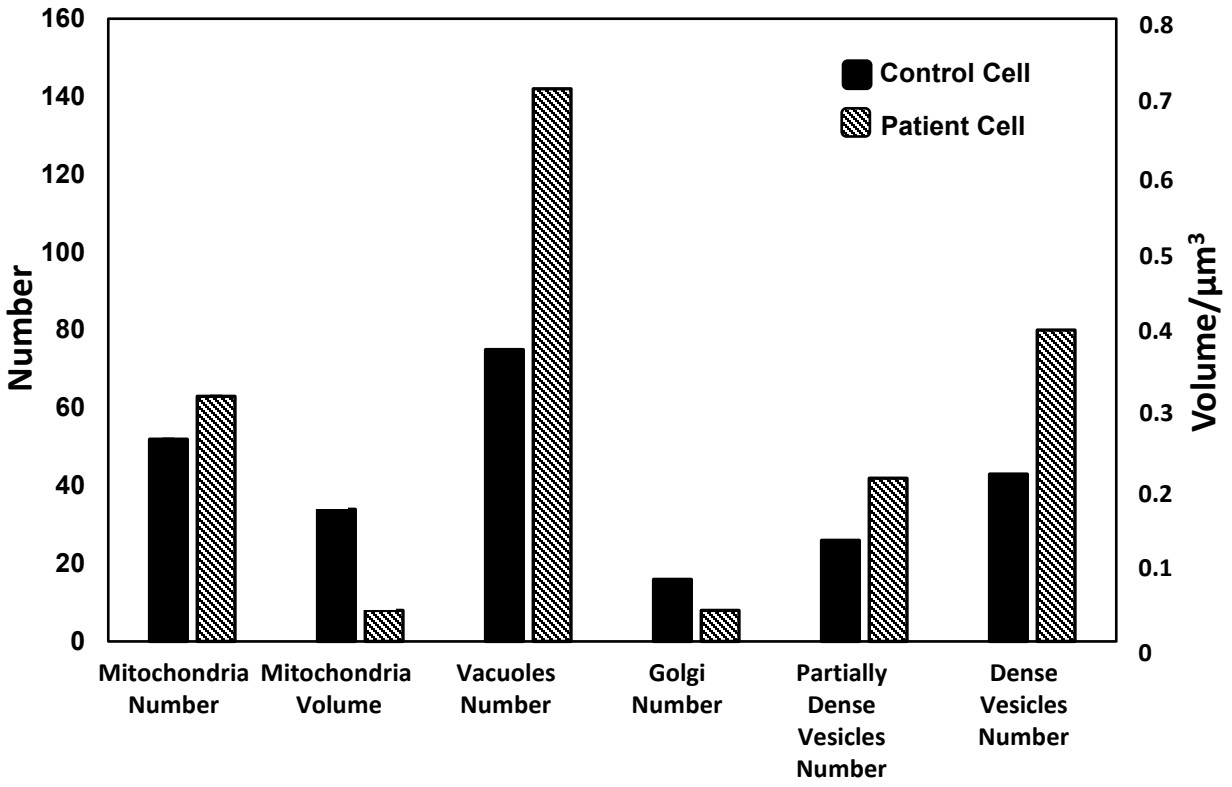

Figure S3 | Number and volume of different organelles in control and patient cells. Related to Figure 3.

Table S1: Summary of serial cryoFIB/SEM parameters. Related to STAR☆Methods, Methods Details, Serial cryoFIB/SEM section.

	FIB Probe current (pA)	SEM Probe current (pA)	SEM acceleration potential (keV)	Dose pA*nS /Å²	Dwell time (ns)	Line averaging count	Pixel size x-y-z (nm)	Image size x-y (pixel)	No. Slices	Volume (µm³)	Time (h:m)
Patient	700	35	2.3	21.3	100	61	10.5 x 10.5 x 21.0	4096 × 3072	2018	50,784	17:20
Control	700	59	1.9	22.4	200	19	10.0 x 10.0 x 20.0	3072 × 1150	575	4,062	5:40